Dieses Dokument ist eine Zweitveröffentlichung (Postprint) /

This is a self-archiving document (accepted version):

Iurie Curosu, Erjon Muja, Mansur Ismailov, Ameer Hamza Ahmed, Marco Liebscher, Viktor Mechtcherine

An experimental-analytical scale-linking study on the crack-bridging mechanisms in different types of SHCC in dependence on fiber orientation

Diese Version ist verfügbar / This version is available on:

https://nbn-resolving.org/urn:nbn:de:bsz:14-qucosa2-838218

SLUB
Wir führen Wissen.

TECHNISCHE UNIVERSITÄT DRESDEN

Qucosa
Quality Content of Saxony

An experimental-analytical scale-linking study on the crack-bridging mechanisms in different types of SHCC in dependence on fiber orientation

Iurie Curosu [*], Erjon Muja, Mansur Ismailov, Ameer Hamza Ahmed, Marco Liebscher, Viktor Mechtcherine

Institute of Construction Materials, Technische Universita¨t Dresden, 01062 Dresden, Germany

ARTICLE INFO

ABSTRACT

A scale-linking, experimental study complemented by an analytical model was carried out to investigate the influence of fiber orientation on the crack-opening behavior of strain-hardening cement-based composites (SHCC). Three SHCC compositions were investigated with polyvinyl alcohol (PVA) and ultra-high molecular weight polyethylene (UHMWPE) fibers in combination with normal- and high-strength matrices. The micro-mechanical experiments with fiber inclinations of 0°, 30°, 45°, and 60° involved fiber embedment in plain and fiber-reinforced specimens. The experimentally derived micromechanical parameters were input into an analytical crack-bridging model to assess the upscaling accuracy of the micromechanical results by comparing the predicted crack-bridging laws to the single-crack opening behavior of equivalent miniature SHCC specimens with controlled fiber orientation. This study yields new insights into the effect of fiber orientation on the crack-bridging properties of different types of SHCC, assesses the link between micromechanical and composite scale properties, offers a solid experimental basis for refining the analytical models, and developing anisotropic ma- terials models for SHCC in dependence on fiber orientation.

1. Introduction

Strain-hardening, cement-based composites – SHCC, also engineered cementitious composites – ECC, represent a family of short-fiber reinforced mortars with a notable pre-peak tensile ductility and crack control [1]. The strain-hardening and multiple cracking behavior of SHCC under tension is achieved by micromechanically adjusted composition, targeting adequate properties of the polymer micro-fibers and fine-grained cementitious matrices, and favorable fiber-matrix interaction [2,3]. The crack-bridging properties of the fibers in SHCC depend strongly on their distribution and orientation relative to their respective crack-openings and loading directions [4]. In turn, fiber orientation is influenced by the production method and application technology of SHCC, such as by casting, lamination, extrusion, or spraying [5–8].

The collective crack-bridging effectiveness of the fibers in SHCC under tension decreases if their orientation deviates from the crack-opening direction. At the single-fiber level it appears that the increase in angle of inclination relative to the crack-opening direction enhances pullout resistance but decreases the *in-situ* tensile strength of the fibers. The first mechanism is denoted as the snubbing effect exhibited by a flexible fiber with negligible bending stiffness passing through a frictional pulley. The strength reduction effect can be traced back to the strong, localized bending and the pronounced surface damage of the fibers at their exit points from the matrix [9]. The effect of fiber inclination on pullout behavior is typically quantified by the snubbing coefficient f for bond strength and the strength reduction coefficient f' for *in-situ* fiber tensile strength. These factors are included in exponential factors of the form $e^{f\Phi}$ next to the reference bond strength and $e^{-f'\Phi}$ next to the reference fiber strength, where reference corresponds to 0° inclination and Φ is the inclination angle in radians [10,11]. The snubbing coefficients are derived from single-fiber pullout experiments, and they depend strongly on the type of fiber and matrix. Li et al. [9] derived a snubbing coefficient of 0.99 for nylon fibers and 0.70 for polypropylene fibers with relatively large diameters of 0.508 mm. Kanda and Li [12] derived a strength reduction coefficient of 0.3 for polyvinyl alcohol (PVA) fibers with two different diameters of 14 μm and 40 μm, while Wu [13] derived snubbing coefficients ranging between 0.2 and 0.8 for similar fiber-matrix combinations. Based on SHCC with relatively thick PVA fibers, *i.e.*, diameter 100 μm, Ozu et al. [14] derived a snubbing coefficient of 0.5 and a strength reduction coefficient of 0.3. Ranade

et al. [15] and Lei et al. [16] derived a snubbing coefficient of 0.59 for ultra-high molecular weight polyethylene (UHMWPE) fibers embedded in a high-strength matrix.

The single-fiber pullout experiments with microfibers typically used in SHCC exhibit certain limitations in deriving the bond parameters as a function of fiber orientation. The main reasons for that are the pronounced scattering of the pullout curves, the occurrence of matrix spalling at the exit point of the inclined fibers, and the premature fiber rupture with increasing fiber inclination. Although fiber rupture can be avoided by using thicker fibers [17], such fibers are not necessarily representative for SHCC systems, which incorporate micro-fibers with diameters ranging from 13 µm to 40 µm [18,19]. Finally, the few reported studieson thistopic focus onspecific materials and offerno scale-linking experimental basis for the refinement and validation of analytical crack-bridging models [20–23].

The aim of this study is to fill this experimental gap by performing a systematic and comprehensive series of scale-linking mechanical investigations at the single-fiber and single-crack levels on three different types of SHCC made with PVA and UHMWPE fibers. The micromechanical experiments as performed pointed to an enhanced methodology regarding their accuracy in characterizing the crack-bridging mechanisms in dependence on fiber orientation. One of the main improvements is related to the preparation of the specimens, where the fiber inclination is reached in stable fashion by rotating the embedment specimens themselves relative to the loading direction, enabling constant, consistent fiber embedment. Another important novelty of the study is related to the incorporation of dispersed fibers in the embedment specimens, in this way enabling a direct comparison to the equivalent SHCC specimens. The latter implied identical volume fractions of fibers and yielded controlled, almost unidirectional fiber orientations of 0°, 30°, 45° and 60°. The geometry and dimensions of the miniature SHCC specimens eliminated structural and size effects, allowing direct comparison with the idealized crack-bridging relationships derived in the analytical model. The fiber orientation in the SHCC specimens was quantified by X-ray micro-computed tomography (µCT) and deep-learning semantic segmentation [24,25]. The experimentally derived micromechanical parameters were input in the analytical crack-bridging model and the predicted collective crack-bridging laws were directly compared to the tensile stress-displacement relationships of the miniature, notched SHCC specimens.

2. Materials

The fiber-matrix combinations investigated in the presented study were aimed at covering typical normal- and high-strength SHCC compositions. The high-performance polymer fibers under investigation were made of PVA and UHMWPE, in short – PE, and their properties are summarized in Table 1 according to the manufacturers [26,27]. Note that the effective fiber diameters as indicated in Table 1 were measured

by means of environmental scanning electron microscopy (ESEM). The fiber lengths varied according to their role in the experiments performed, as described in Sections 3.1 and 3.2. PVA fibers are used most commonly in normal-strength SHCC due to their hydrophilic surface properties and moderate *in-situ* tensile strength [12,19]. On the other hand the PE fibers are hydrophobic and form only a frictional and mechanical anchorage in cementitious matrices [18]. As opposed to the PVA fibers, which exhibit pronounced slip-hardening pullout behavior due to surface scratching and jamming inside the matrix channel [12,28], the PE fibers exhibit controlled frictional pullout behavior [15,18,29].

Table 2 presents the matrix and SHCC compositions under investigation. These are valid both for the single-fiber pullout specimens (Section 3.1) and for the miniature SHCC specimens (Section 3.2).

As in previous works by the authors, M1 is the designation of the normal-strength matrix, and M2 implies a high-strength matrix [30,31]. The normal-strength matrix was originally developed for the hydrophilic PVA fibers, explaining its high content of fly ash. The relatively large particle size of fly ash [32] and its low hydration rate limit the packing density of the M1 matrix and the bond strength with the PVA fibers. Despite the composition of the M1 matrix and the oil coating of the PVA fibers, the hydrophilic surface properties of the fibers and their relatively low abrasion resistance led to fiber rupture after a limited extent of pullout, even with embedded lengths of 2 mm [19,30,33].

Due to their higher aspect ratio as compared to PVA, the PE fibers led to a more pronounced reduction in the flowability of the fresh SHCC, requiring a slightly higher dosage of superplasticizer in M1-PE; see Table 2. Otherwise, the matrix composition is identical to that of M1-PVA. The frictional bond strength of the PE fibers in M1 is rather low at a curing age of 14 days and only a very limited extent of fiber rupture occurs in M1-PE with typical fiber lengths of up to 12 mm [30].

Given their higher tensile strength, the PE fibers can ensure adequate crack-bridging performance as well in high-strength matrices such as M2, which has a substantially higher content of cement and, in turn, a lower water-to-cement ratio. Silica fume is used as a partial cement replacement, and the content of fine sand is considerably lower when compared to M1. This composition ensures a high packing density and strong fiber anchoring.

3. Experimental program

3.1. Single-fiber pullout experiments

One of the important features of the single-fiber pullout tests in this work is the involvement of fiber-reinforced specimens in addition to the plain matrix specimens. This was aimed at improving the upscaling accuracy of the experimentally derived micromechanical parameters concerning the crack-bridging mechanisms in SHCC. The dispersed fiber

Table 1
Geometric and mechanical properties of PVA and PE fibers according to the manufacturers [26,27]. The effective fiber diameters were measured by ESEM, and the standard deviations are given in parentheses next to the average values.

Fiber	PVA	UHMWPE
Producer, country	Kuraray, Japan	DSM, the Netherlands
Brand	Kuralon REC15	Dyneema SK62
Diameter (µm)	38 (2 4)	18 (1 3)
Length[a,b,c] (mm)	8[a], endless[b], 12[c]	6[a], endless[b], 12[c]
Density (g/cm^3)	1 26	0 97
Tensile strength (MPa)	1600	2500
Young's modulus (GPa)	40	80
Elongation at break (%)	6 0	3 5

[a] As dispersed fibers in single-fiber pullout experiments (Section 3.1).

[b] As loaded fibers in single-fiber pullout experiments (Section 3.1).

[c] As dispersed fibers in tension experiments (Section 3.2).

Table 2
Mixture composition of the SHCC under investigation and of the corresponding plain matrices M1 and M2 with no added fibers.

Component (producer, country)	M1-PVA	M1-PE	M2-PE
CEM I 42 5 R-HS (Schwenk, Germany)	505	498	–
CEM I 52 5 R-SR3/NA (Holcim, Germany)	–	–	1460
Fly ash Steament H4 (Steag Power Minerals, Germany)	621	612	–
Silica fume Elkem 971 (Elkem, Norway)	–	–	292
Quartz sand 60–200 µm (Strobel Quarzsand, Germany)	536	529	145
Viscosity modifying agent (SIKA, Switzerland)	4 8	4 7	–
Water	338	333	315
Superplasticizer Glenium ACE 30 (BASF, Germany)	10		
Superplasticizer Glenium ACE 460 (BASF, Germany)	–	25	35
PVA fiber, 1 0% by vol (Kuraray, Japan)	13	–	–
PE fiber, 1 0% by vol (DSM, the Netherlands)	–	10	10

reinforcement was expected to limit the extent of matrix spalling with increasing fiber inclination, in this way allowing a more accurate assessment of the effect of fiber inclination on the bond strength. Also, according to Kanda and Li [12] and Yang et al. [34], the apparent bond strength of the PVA fibers inplain matrices is higher than in SHCCdue to the increased air content in the latter. This being so, the authors intended to verify this effect in different types of SHCC.

The molds and production steps of the single-fiber pullout specimens are presented in Fig. 1. The high consistency and limited flowability of the fiber reinforced paste did not permit one-step casting. For this reason, the main fibers were first placed on the ventral side of the top plates and fixed with wax as shown in Fig. 1a. The fibers were placed parallel to each other at a spacing of approximately 10 mm and bridged the longitudinal channel perpendicular to it. In the initial step the channel was only filled up to the top edge of the support plates, *i.e.*, half the effective channel depth. Subsequently, the top plates together with the fibers were placed over the molds and fixed in position by screws as shown in Fig. 1b. Finally, the second half of the channel was filled with the fiber reinforced paste. Casting was done on a vibrating table.

In the case of the plain matrix specimens, the fibers were placed directly onto the support plates as shown in Fig. 1c. The high flowability of the plain pastes allowed the filling out of the mold without slacking the fibers or forming large air inclusions. The entrapped air was partly extracted by the vibration of the molds during casting.

Because of the pronounced negative effect of the dispersed fibers on the flowability of SHCC, the fiber content and length in the pullout specimens were limited toextents allowing adequatequality of the small pullout specimens. The fiber volume fraction was 1% for all combinations, identical to the fiber content in the miniature SHCC specimens for tension experiments as described in Section 3.2. The shortest available fibers were selected as dispersed reinforcement for the embedment specimens. The dispersed PVA fibers were 8 mm long and the PE were 6 mm long. The main, *i.e.*, loaded, PVA and PE fibers were cut to lengths of 100 mm from endless filaments and their length ensured sufficient anchorage in the glue.

The resulting specimens represent slender beams with thickness defining the embedded length of the fibers, which protrude transversely out of the samples. The embedded length was defined by the spacer plates as shown in Fig. 1c. These samples were cut transversely between the neighboring fibers, resulting in widths of approximately 6 mm to 8 mm and embedded lengths of either 2 mm or 6 mm. In the case of M1-PVA and M2-PE, 2 mm embedment was intended to assess the bond properties, while the 6 mm embedment targeted mainly fiber rupture and assessment of the fiber tensile strength *in-situ*. In the case of M1-PE, the pullout experiments require an embedded length of 6 mm for the proper evaluation of bond strength [30]. The fiber-matrix combinations for the testing configuration of 0° inclination, including the type of embedment material and embedded length, are presented in Fig. 2.

Fig. 3 presents the testing configuration with two M1-PE specimens at 6 mm embedment and at inclination angles of 0° and 30°, respectively. The embedded pieces were glued onto steel screws and mounted on the support elements made of plastic. Prior to gluing, the protruding fiber on the respective face was cut off and the remaining spot was covered with wax to avoid possible contact between glue and fiber tip. The free length of the fibers in these experiments was approximately 4 mm. Loading of the fiber occurred in an electromechanical testing machine, a Zwick 1445 (ZwickRoell, Germany), in a displacement-controlled regime at a displacement rate of 0.05 mm/s. The 10 N capacity force transducer, an HBM U1A (HBM, Germany), was installed between the cross-member and the aluminum plate onto which the fibers were glued using X60 glue obtained from HBM (Germany).

Note that the fiber inclination was not provided by placing the fibers skew in the molds as commonly done in the studies reported [12,15,16], but by rotating the specimens relative to the loading axis; see Fig. 3. Such method ensures constant embedded length of the fibers, independent of the inclination angle. In case of rotated fibers in the mold, the increase in inclination results in a greater embedded length, which has an additional effect on the apparent bond strength [16,35].

The inclination angles under analysis were 0°, 30°, 45°, and 60°. Given the pronounced scattering of the results typical for such experiments, at least 10 specimens were tested for each parameter combination. Curing of the specimens involved 13 days in sealed plastic bags, stored in a climatic chamber at a constant temperature of 20 °C and a relative environmental humidity of 65% RH. The age at testing was 14 days, which was logistically imposed by the large number of performed experiments. This age also allowed a direct comparison with previous studies by the authors [18,30,31].
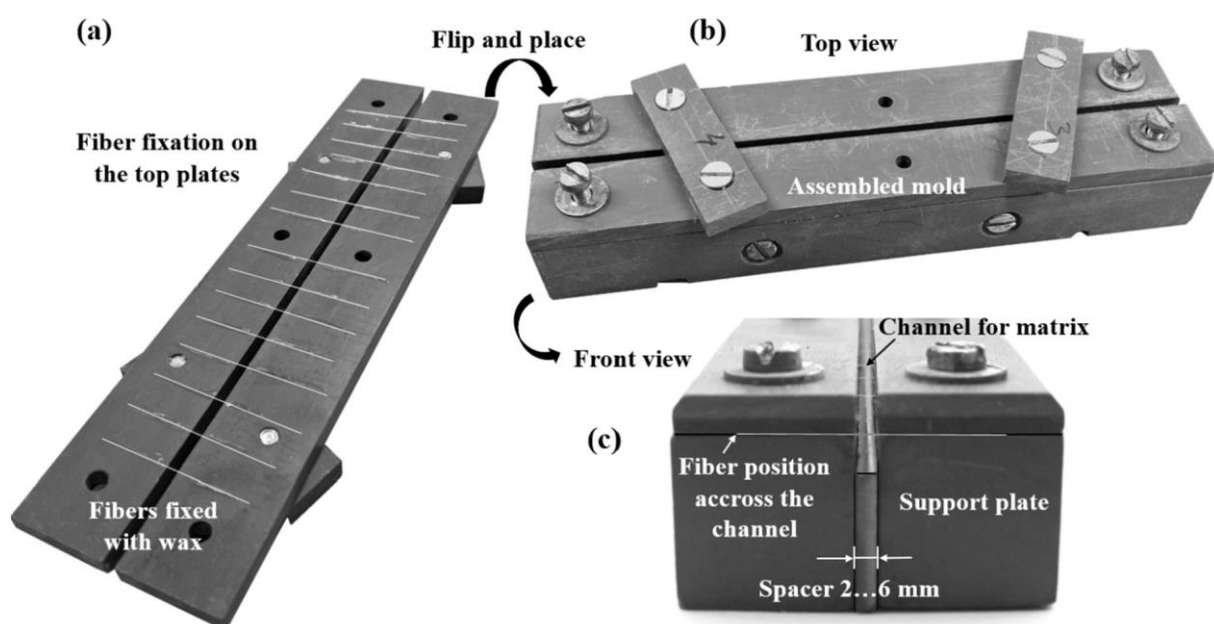

Fig. 1. Mold for single fiber-pullout specimens with clamped fibers prior to filling out the channel with plain or fiber reinforced paste. The fibers are highlighted in white for improved visibility.
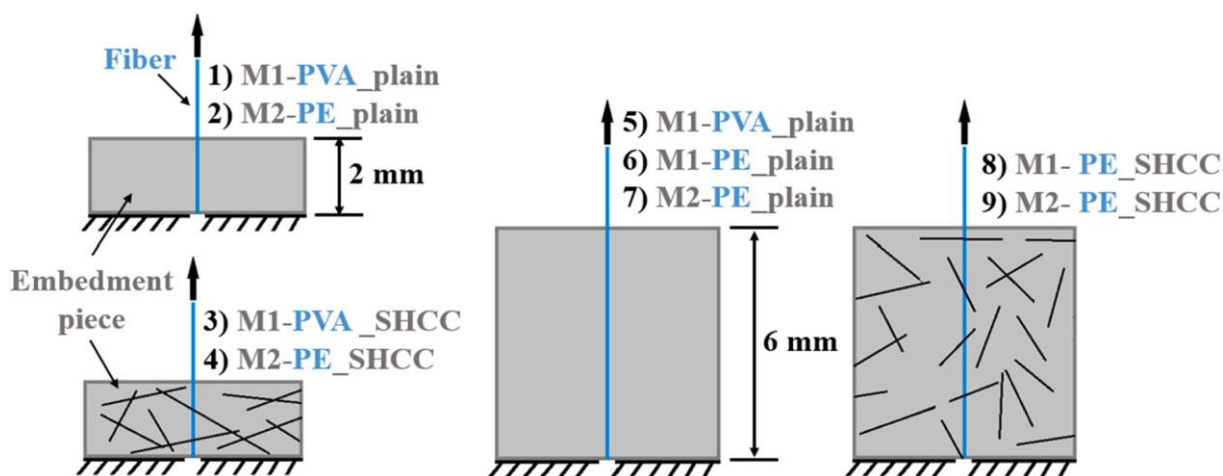
3

Fig. 2. Material combinations and embedded lengths investigated in single-fiber pullout experiments.
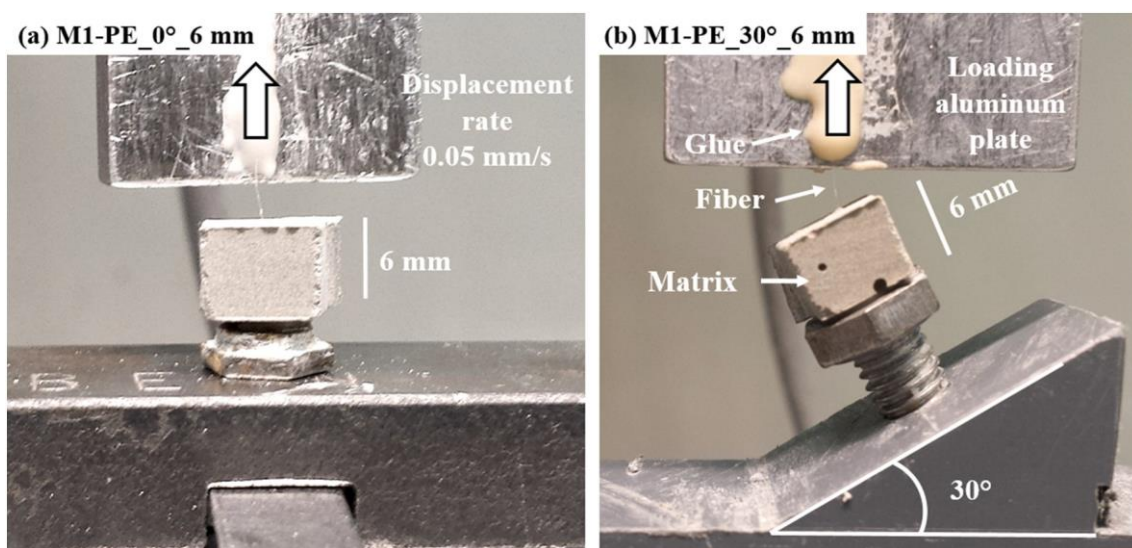

Fig. 3. Setup for single-fiber pullout experiments. Example showing M1-PE specimens with an embedded length of 6 mm and inclination angles of (a) 0° and (b) 30°.

3.2. Tension experiments on miniature SHCC specimens

To link the experimentally derived micromechanical parameters accurately to the collective crack-bridging features typical for SHCC, miniature SHCC specimens were produced and tested under tension. These specimens had the same volume fraction of short fibers as the pullout specimens, *i.e.*, 1%, while their production technique and small thickness allowed proper control of the fiber orientation. Concurrently the size, shape, and presence of notches in the SHCC specimens limited the influence of various structural effects, in this way offering a tailored experimental basis as comparison to the idealized analytical model of single-crack opening.

These specimens were initially designed to generate an experimental basis for 2D numerical models of SHCC with discrete fiber reinforcement [36] and their production technique was described in detail in previous works by the authors [24,25]. Special molds were fabricated for 40 mm wide, dumbbell-shaped specimens with a thickness in the gauge portion of approximately 3 mm. Such a small thickness was ensured by pressing a top mold element into the cast SHCC, causing a longitudinal displacement of the fresh SHCC towards the ends of the mold and, additionally, longitudinal fiber orientation [24,25]. The geometric properties with a schematic representation of fiber orientation in the donor, plate-like samples are presented in Fig. 4. These were cured for

10 days under identical conditions as the pullout specimens. For this study only the thin gauge portion of the dumbbell-shaped samples was of relevance. The miniature specimens were extracted by cutting 10 mm- wide strips at various angles as shown in Fig. 4 to achieve the desired fiber orientation.

The specimen length was 45 mm. Notches were cut laterally in the middle of the specimens to ensure one single crack in the uniaxial tension experiments. The notches were cut with a 1.5 mm-thick circular saw, and their depth was approximately 2 mm. The specimens are presented in Fig. SI1 in Support Information (SI) with M1-PVA as an example. Prior to mechanical testing, the thickness of the specimens and the width of the effective cross-sections were measured, and the specimens were scanned in an X-ray μCT for evaluating the effective fiber orientation; see Section 3.3.

The length of the dispersed fibers was 12 mm in all types of SHCC. At least four specimens were tested for each parameter combination in an electromechanical testing machine, a ZwickiLine (ZwickRoell, Germany), under a displacement rate of 0.05 mm/s. A built-in force cell type, an Xforce P of load capacity 2.5 kN, was used to measure the load. The specimens were glued to aluminum plates using X60 glue, leaving a free length of 10 mm, as shown in Fig. 4. The boundary conditions in terms of rotation capacity were semi-rigid. Since measuring the crack-opening history by mechanical means was not possible, the
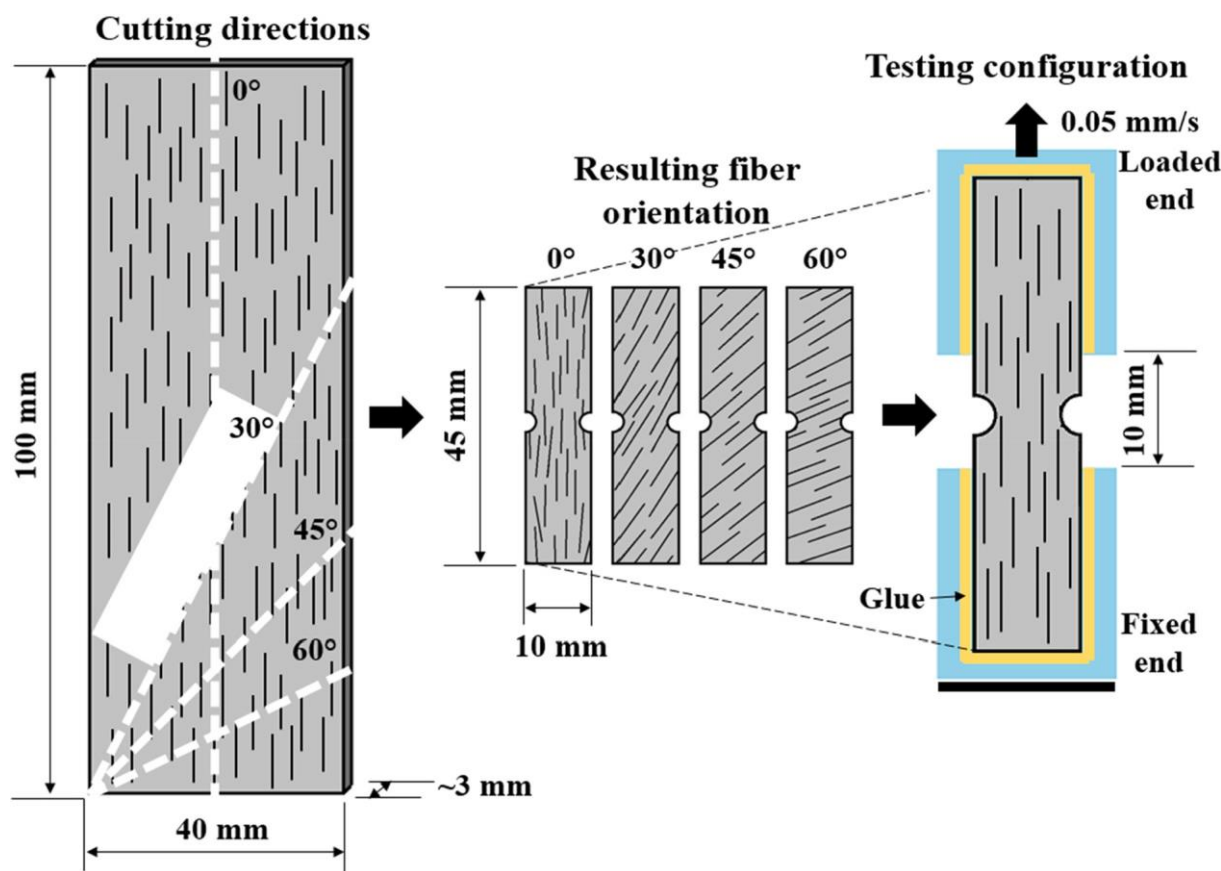
Fig. 4. Production, fiber orientation, and testing configuration of miniature SHCC specimens.

displacement of the cross-member was recorded to approximate the crack-opening histories, the latter including the compliance of the testing setup.

The state of the fibers on the fracture surfaces of the tested SHCC samples was assessed by means of ESEM in a Quanta 250 FEG (FEI, USA) microscope without applying an additional sputter coating.

3.3. X-ray μCT scanning and fiber segmentation

The fiber orientation in the miniature SHCC specimens was assessed by means of X-ray μCT using a CT-XPRESS model (ProCon X-ray GmbH, Germany) coupled with an X-Tom software for scanning. The X-ray voltage was 72 kV, and the current was 200 μA. The exposure time was 0.18 s, averaging three projections to record the result. The small specimen cross-section facilitated a small distance between the specimen and the X-ray source, thus enabling the large geometric magnification of the specimen and high pixel accuracy. With a binning of 1×1, the resulting voxel size ranged between $(4.6^3 \ \mu m^3)$ and $(4.8^3 \ \mu m^3)$, yielding 2160 projections. The reconstruction of the CT volumes was performed in VG Studio Max 3.2 (Volume Graphics, Germany).

The same as in previous studies by the authors [24,25], the semantic segmentation of the fibers was performed in the software Dragonfly version 4.0 by TheObjects (Canada) employing deep learning. To enhance the segmentation accuracy of the fibers in the reconstructed 2D slices, additional pre-processing steps were carried out, such as histogram clipping and mean filtering. The training data for the neural network was prepared by manually labeling the phases of interest on the reconstructed 2D slices. Based on the training set as generated, the neural network defined the mappings for the automatic segmentation of μCT slices of similar structure. Two specimens were scanned per parameter combination. This segmentation provided a detailed statistical assessment of fiber orientation in the gauge portions of the

specimens. The data on fiber orientation were used as input in the analytical crack-bridging model.

4. Crack-bridging model

Analytical crack-bridging models are aimed at predicting the single-crack opening behavior of SHCC based on the constituents' properties and are useful in optimizing material [37,38]. The models are based on the kinematics of fiber slippage relative to the surrounding matrix. The input parameters are the geometric and mechanical properties of the fibers, the mechanical properties of the matrix, the fiber volume fraction, the statistically distributed embedded length and orientation angle, and the empirical factors accounting for fiber inclination [39], rate effects [15], fiber rupture [39], and matrix spalling [34].

In this study, the main role of the analytical model is to assess the scale-linking accuracy of the experimentally derived micromechanical parameters. The collective crack-bridging model assumes an individual analysis of the crack-bridging fibers similar to the approach proposed by Jun and Mechtcherine [40] and a statistical consideration of the fiber and bond properties [32]. The advantage of this approach as compared to the integration method, such as proposed by Li et al. [41], is that fiber rupture can be accounted for in a direct way and a random distribution can be easily attributed to each material or composite parameter. In the work at hand, the single-fiber, crack-bridging relations were adopted from the works of Lin and Li [42] and Lin et al. [43]. In the case of 0° fiber orientation, the number of fibers n_f generated depends on the given fiber volume fraction V_f in the SHCC and in a certain analyzed cross-section of area A_{cs}. With increasing fiber inclination in the miniature SHCC specimens, the effective number of fibers crossing the orthogonal middle cross-section decreases on average according to the $\cos(\Phi)$, as shown in Eq. (1), where Φ is the global inclination angle of the fibers. The number of fibers analyzed also defines the number of

calculation loops in a simulation.

$$n_f = V_f \cdot \frac{A_{cs}}{A_f} cos(\Phi) \qquad (1)$$

Each generated fiber is subject to a number of displacement steps of size $\delta = 0.001$ mm; their number equals the half-length of the fibers divided by the size of the displacement step. At each incremental displacement step δ, the stresses in the fiber under analysis and at the interface are verified according to Eqs. (2) through (4), and the pullout forces derived are recorded as a function of displacement, generating for each fiber a two-column vector, *i.e.*, force and crack-opening, which are finally summed up in deriving the collective crack-bridging relationships. The force-crack opening relation for a single fiber before complete interfacial debonding or before reaching the tensile strength of the fiber is calculated according to Eq. (2):

$$P(\delta) = e^{f\Phi} \sqrt{(\tau\delta + G_d) \cdot \pi^2 E_f d_f^3 / 2} \qquad (2)$$

in which δ is the displacement resulting from the debonding of the fiber on both crack flanks, τ is the frictional bond strength, G_d is the chemical bond, E_f is the fiber stiffness, and d_f the diameter. The exponential function is the snubbing factor, which accounts for the effect of fiber inclination on the apparent bond strength. The force at which complete debonding occurs is calculated according to Eq. (3):

$$P_{debonding} = e^{f\Phi} \left| \pi d_f \tau L_e + \sqrt{G_d \pi^2 E_f \frac{d_f^3}{2}} \right| \qquad (3)$$

in which L_e is the embedded length of the given fiber on the shorter side. If the bond strength is exceeded and the fiber does not fail before complete debonding, the forces at larger displacements are calculated according to Eq. (4):

$$P(\delta) = \pi\tau d_f(1 + \beta_{sh}(\delta - \delta_0))(L_e - (\delta - \delta_0))e^{f\Phi} \qquad (4)$$

where δ_0 is the displacement at complete debonding and β_{sh} is the slip-hardening coefficient. In the case of reaching the *in-situ* tensile strength of the fiber, the crack-bridging forces vanish at larger crack openings. Two-sided debonding and one-sided pullout were considered.

The model involved a constant set of parameters, *i.e.*, values equal for the entire set of fibers, and a statistical one, *i.e.*, different values for each fiber. The parameters serving as input in the model are given in Section 6 including the values derived in single-fiber pullout experiments in this work and in [32].

To account for the reduction in apparent bond strength with increasing embedded length [35,44], an adjustment function was applied based on the results of Boshoff et al. [35] as shown in Eq. (5):

$$Bond_{adj} = \left(\frac{L_e}{L_{e\_reference}}\right)^{-0.4} \quad (\text{for } L_e \geq 1) \qquad (5)$$

Due to the lack of experimental evidence, no adjustment was applied to embedded lengths smaller than 1 mm. The denominator, the reference embedded length, is 2 mm for M1-PVA and M2-PE and 6 mm for M1-PE according to the embedded lengths applied in the pullout tests.

5. Results and discussion

5.1. Single-fiber pullout experiments

The titles of the single-fiber pullout diagrams indicate the matrix, M1 or M2, and fiber, PVA or PE, combination followed by the inclination angle of the fibers in degrees, subsequently by the embedded length of the fibers and the type of embedment material, *i.e.*, either plain matrix or SHCC.

The pullout curves of PVA fibers in plain matrix M1 in Fig. 6 exhibit a slip-hardening pattern with fiber rupture after only a short pullout phase. The initial force peaks before entering the pullout phase represent chemical debonding instances [12], which can occur multiple times prior to pullout initiation. This is caused by the excessively strong bond
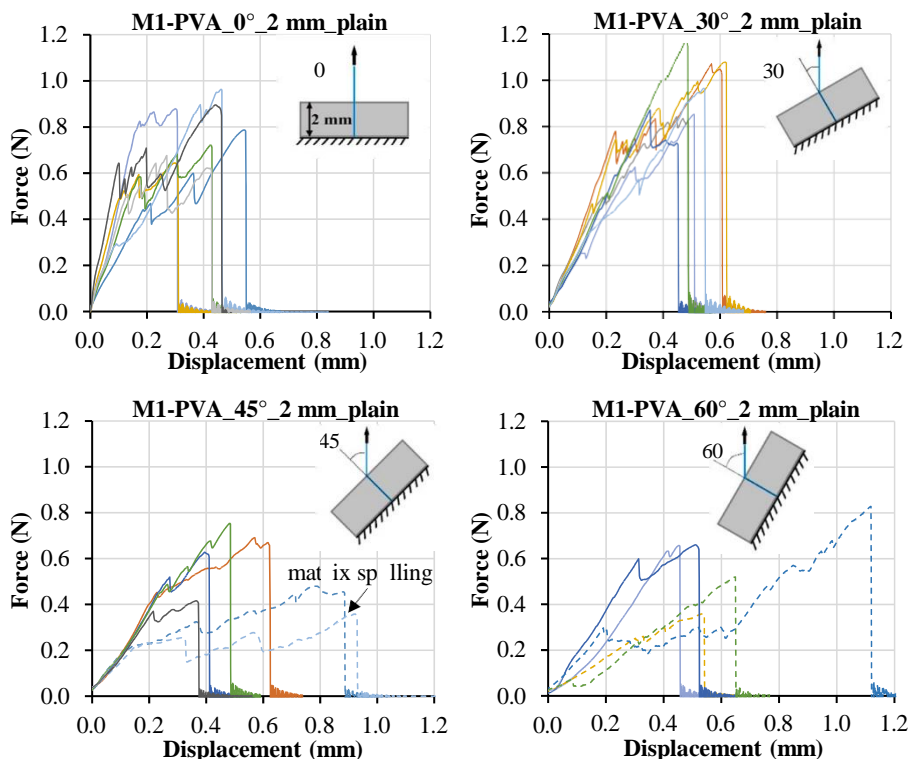

Fig. 6. Pullout curves of single PVA fibers at different inclination angles in plain matrix M1. The embedded length is 2 mm.

developed by the hydrophilic PVA fibers despite the additional oil coating [33]. The pullout load after complete debonding is controlled only by the frictional bond and mechanical interlock caused by the cohesive interphase failure and fiber surface damage [28]. Most of the curves do not exhibit a definite transition from the debonding stage to the pullout phase and do not enable an accurate derivation of the chemical bond strength according to the fracture mechanical approach, as given in Eq. (6) [43]:

$$G_d = \frac{2 \cdot \Delta P^2}{\pi^2 \cdot E_f \cdot d_f^3}$$

(6)

in which ΔP is the difference between the force peak at complete debonding in the case of one single debonding instance and the initial load at frictional pullout initiation. For this reason, the chemical bond will be approximately derived by a parameter fitting in the analytical model presented in Section 6.

The frictional bond is determined according to the simplified, strength-based approach assuming a uniform shear stress distribution along the embedded fiber. It is calculated as the ratio of the force at initiation of pullout to the embedment surface of the fibers as in Eq. (7), with the average fiber diameters given in Table 1.

$$\tau = \frac{P_f}{\pi \cdot d_f \cdot L_e}$$

(7)

The resulting average bond strength of the aligned PVA fibers in the plain M1 matrix is given in Table 3 and is very close to that derived for an identical fiber-matrix combination in previous works by the authors [19,30]. The average bond strength increases at 30° inclination and decreases at 45° and 60° inclination. As a result, the snubbing coefficient f has a negative value of −0.09, which contradicts the results reported in the literature so far [12,13,14]; see Fig. 8a. However, the average values for inclinations of 45° and 60° as summarized in Table 3 have a lower statistical significance since several curves in Fig. 6 obviously indicate matrix spalling.

Based on the experiments visualized in Fig. 6, the in-situ tensile strength of the PVA fibers yields an unsteady trend as well, being 677 MPa for 0°, increasing to 864 MPa for 30° and decreasing to 503 MPa for 45° and increasing again to 534 MPa for 60°. The large difference between the nominal tensile strength of PVA fibers and their in-situ tensile strength is also known from previous studies and is caused by the substantial surface damage occurring in the pullout phase [19,30].

To limit the extent of slip and derive the in-situ tensile strength representative of larger embedded lengths, pullout experiments out of the plain M1 matrix were performed with an embedded length of 6 mm. The corresponding curves are presented in Fig. SI2 in SI and the results are summarized in Table 3. The limited slip and lack of matrix spalling at 45° and 60° fiber inclination resulted in higher in-situ tensile strengths than with 2 mm embedment, and the trend indicates no negative influence of inclination angle; see Table 3 and Fig. 8b.

Fig. 7 presents the pullout curves corresponding to fiber reinforced specimens, i.e., embedment in SHCC. The reason for the unsteadiness of the 0° curves is not clear, but it could be related to matrix inhomogeneity around the fiber, although this assumption is not reflected in the results

at larger inclinations. Only two curves enabled an accurate assessment of the apparent bond strength at 0°, the values being 0.75 MPa and 2.43 MPa. At 30° the average bond strength was 2.34 MPa, undergoing reductions to 1.98 MPa for 45° and 1.87 MPa for 60°. In the case of 60°, the shallower ascending branches could be traced back to the flexural deformation of the fibers. No pronounced negative effect of dispersed fiber on the bond strength can be deduced when compared to the plain matrix, as shown in Table 3, and the resulting trend with inclination angle in radians yields a snubbing coefficient of 0.27; see Fig. 8a. Both with and without short fiber reinforcement, the bond strength increases at 30° and then decreases with increasing inclination angle. Note that the exponential trendline is not accurately representative of the influence of fiber orientation. Nevertheless, the exponential snubbing factors are considered in this work to enable direct comparison with the published results on this matter.

The in-situ fiber tensile strength follows a similar trend as the experiments with plain matrix and 6 mm embedment as in Fig. SI2 and yielded no global reduction in tensile strength compared to 0° inclination, meaning that the strength reduction coefficient f' is 0.0 in this range of inclination angles; see Fig. 8b. Given the pronounced fiber surface damage caused by the cohesive failure, it seems that the additional contribution of the fiber inclination to strength reduction is not decisive.

The pullout curves of PE fibers in the plain, normal-strength matrix are presented in Fig. 9 and show that the pullout resistance decreases with inclination angle.

The trend is consistent despite the pronounced scattering of the curves. Due to the low pullout forces at larger inclinations, no matrix spalling occurred. Furthermore, the scattering of the curves is reduced substantially with the increasing inclination angle. The ultimate pullout displacements extending beyond the actual embedded length of the fibers could be a result of imperfect mold dimensions, of the initial nonstretched state of the fibers, and of their flexural deformation with increasing inclination.

If M1-PE is used as embedment material instead of the plain M1 matrix, a shift of the failure mode towards fiber rupture can be observed, becoming more pronounced with increasing inclination angle; see Fig. 10. Although an effect of the dispersed short fibers on the air content is plausible, there should be other concurrent effects which lead to an increase in bond strength as compared to plain matrix. One of the reasons could be related to the positive effect of the fibers on particle dispersion during the mixing process and, hence, on the degree of binder hydration. Another reason could be related to the increased global specific surface of the system due to the dispersed micro-fibers, in this way reducing the thickness of the water film around the loaded fibers in M1-PE when compared to those embedded in M1. Note that this effect might be different in the case of hydrophilic PVA fibers.

Since the occurrence of fiber rupture is more pronounced with an increase in inclination angle in the case of M1-PE as embedment material, the frictional bond strength could not be reliably assessed. Table 4 presents the derived values of bond strength, for which also the failure forces of the fibers were taken into account. Although this yields superior accuracy compared to the case in which only the pulled out fibers are considered in the statistical analysis, the effective bond strength is still underestimated since actual pullout would occur at larger forces if the fibers did not fail. The actual bond strength for M1-PE embedment, for which pullout mostly occurred, is reliable for 0° inclination and will be used in the analytical model as a reference. Compared to the values derived in the authors' previous work [30], the bond strength for 0° in this study is multiple times higher, which could be traced back to the quality of the specimens and to deviations in the raw materials' properties over the years.

The diagram in Fig. 11a presents bond strength variation determined in plain matrix and SHCC M1-PE together with the exponential trendlines. It also shows negative snubbing coefficients f of −0.73 in plain matrix and −0.34 in SHCC. As opposed to the PVA fibers, the in-situ

Table 3
Frictional bond strength and in-situ tensile strength of PVA fibers as a function of fiber inclination derived by means of single-fiber pullout experiments in plain matrix M1 and in SHCC M1-PVA. Average values are given with standard deviations in parentheses.

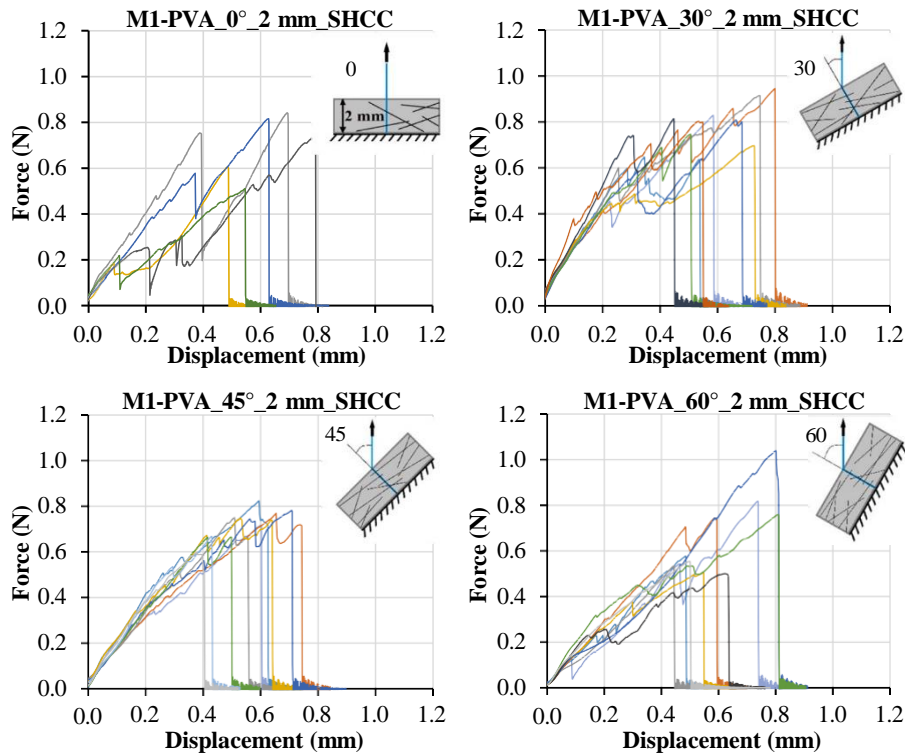| Parameter/fiber angle	0°	30°	45°	60°
τ_2 mm_plain in MPa	2 34 (0 71)	2 60 (0 72)	1 95 (0 27)	2 12 (0 91)
τ_2 mm_SHCC in MPa	0.75/2.43	2 34 (0 43)	1 98 (0 57)	1 87 (0 81)
σ_f_2 mm_plain in MPa	677 (103)	864 (114)	503 (126)	534 (155)
σ_f_2 mm_SHCC in MPa	621 (125)	706 (84)	639 (62)	624 (184)
σ_f_6 mm_plain in MPa	754 (144)	759 (74)	727 (114)	739 (149)

Fig. 7. Pullout curves of single PVA fibers at different inclination angles in SHCC M1-PVA with a fiber volume fraction of 1%. The embedded length is 2 mm.
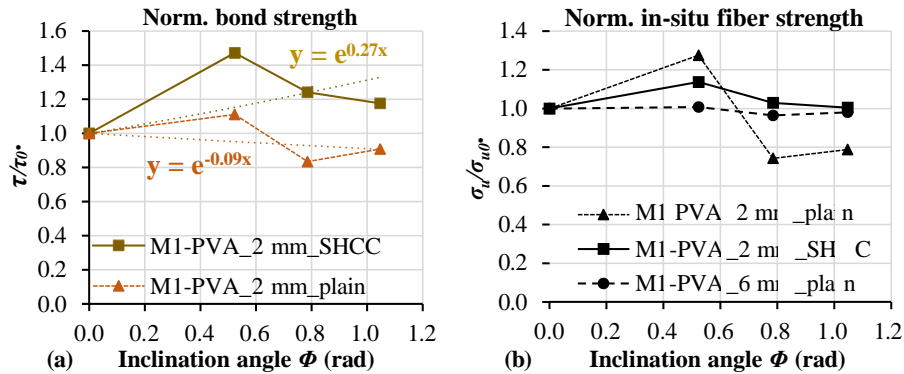

Fig. 8. (a) Normalized average bond strength including the exponential trendlines with the resulting snubbing functions and (b) *in-situ* tensile strength of PVA fiber in plain matrix M1 and in SHCC M1-PVA.

tensile strength of the PE fibers in M1-PE corresponds to the nominal tensile strength; see Table 4. The strength reduction coefficient f' for this fiber-matrix combination as derived in SHCC is 0.18; see Fig. 11b. Hence, the results confirm the findings in the literature regarding the influence of orientation angle on the tensile strength of the PE fibers but contradict those related to the bond strength.

The single-fiber pullout curves of PE out of plain, high-strength matrix M2 and SHCC M2-PE are presented in Figs. 12 and 13, respectively. The curves corresponding to plain matrix yield only scarcely derivable micromechanical parameters due to the very low forces and unsteady patterns present, in which the average bond strength is unrealistically low; see Table 5. At the same time, the difference in bond strength with and without dispersed fibers is even more considerable than among M1 and M1-PE.

Note that the curves derived by the authors in previous works on an identical matrix provided fiber pullout curves with substantially higher pullout loads [18,30]. This emphasizes the high sensitivity of the

micromechanical experiments to variations in terms of production technique, testing configuration, and material inhomogeneity, and to the variation in cement properties as well.

Whereas the results with plain matrix M2 provide no clear trend regarding the influence of inclination angle, those based on SHCC show a clear reduction in bond strength but at the same time the occurrence of fiber rupture at 60° inclination; see Fig. 13 and Table 5. Given the extremely low forces for 2 mm embedment in plain matrix and the impossibility of deriving the *in-situ* fiber tensile strength either in plain matrix or in SHCC, additional experiments were performed with an embedment of 6 mm using plain matrix and SHCC as embedment; see Figures SI3 and SI4 in SI as well as the summarized results in Table 5. The experiments on plain matrix could not provide the apparent bond strength accurately as a function of fiber inclination due to the frequency of fiber rupture at 45° and 60°. On the other hand, with SHCC as embedment material, the excessive fiber rupture allowed only the derivation of the *in-situ* tensile strength; see Table 5.
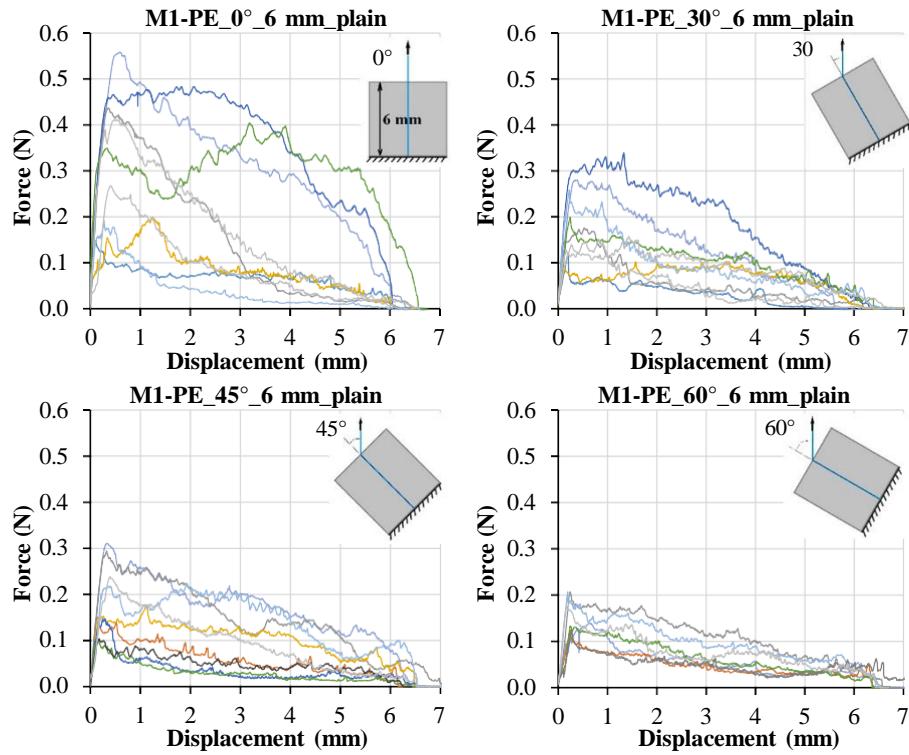
8

Fig. 9. Pullout curves of single PE fibers at different inclination angles in plain matrix M1. Embedded length is 6 mm.
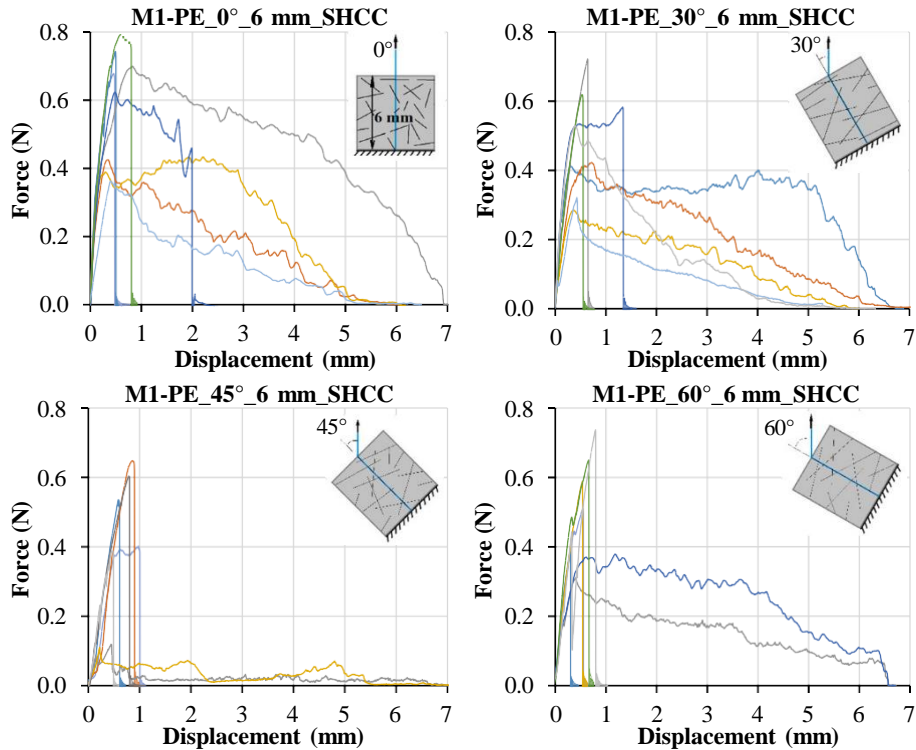

Fig. 10. Pullout curves of single PE fibers at different inclination angles in SHCC M1-PE with 1% fiber volume fraction. Embedded length is 6 mm.

The influence of orientation angle on the apparent bond strength in the case of PE fibers embedded in M2 and M2-PE is presented together with the exponential trendlines in Fig. 14a. The pullout results corresponding to plain matrix and 2 mm embedment are not presented since the curves are obviously not representative of the composite scale. The results obtained in SHCC with 2 mm embedment and plain matrix with 6 mm embedment are contradictory, the first showing a negative snubbing coefficient of $f = -0.35$ and the second one resulting in a positive snubbing coefficient of $f = 0.33$. The objectivity and accuracy of these coefficients regarding the collective crack-bridging properties in

9

Table 4

Frictional bond strength and *in-situ* tensile strength of PE fibers as a function of fiber inclination derived by means of single-fiber pullout experiments in plain matrix M1 and in SHCC M1-PE. Average values are given with standard deviations in parentheses.

Parameter/fiber angle	0°	30°	45°	60°
τ_6 mm_plain in MPa	1 02 (0 43)	0 58 (0 23)	0 57 (0 23)	0 52 (0 18)
τ_6 mm_SHCC in MPa	1 75 (0 48)[a]	1 41 (0 44)[a]	1 18 (0 64)[a]	1 39 (0 39)[a]
σ_f_6 mm_SHCC in MPa	2599 (551)	2521 (285)	2027 (462)	2244 (609)

[a] Also derived based on the fiber failure loads.

SHCC are assessed in the analytical crack-bridging model in Section 6. The resulting strength reduction coefficient is $f' = 0.21$ in Fig. 14b and is slightly different than that derived with normal-strength SHCC

M1-PE ($f' = 0.18$); see Fig. 11b. This increment can be traced back to the higher surface hardness of the high-strength matrix M2 compared to M1 and in turn to the more pronounced fiber surface damage. This can be also assessed based on the slip-hardening character exhibited by some of the curves with increasing inclination angle both in plain matrix M2 and in SHCC M2-PE. Also as summarized in Table 5, the *in-situ* tensile strength of the fibers in plain matrix with 6 mm embedment is considerably lower than in SHCC despite the similar extent of slip.

To shed more light on the results presented in this section, the pullout specimens and fibers were analyzed by optical microscopy, aiming to identify patterns in matrix spalling and fiber surface damage. However, no consistent findings became apparent, and accordingly the global influence of fiber orientation was assessed in experiments at the single-crack level in SHCC, as presented in Section 5.3.
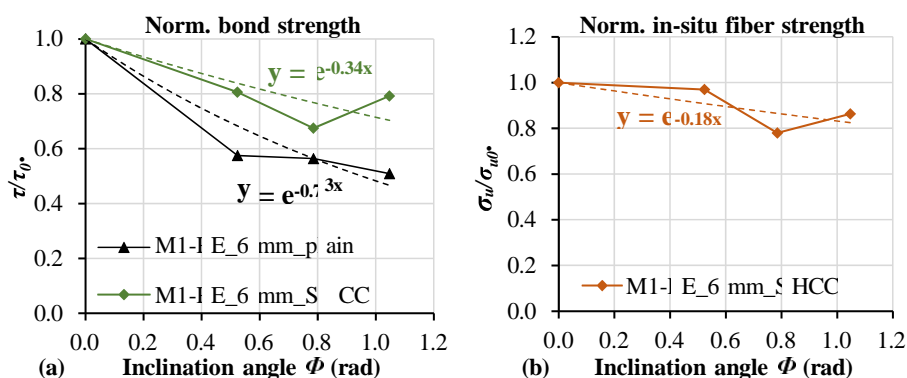

Fig. 11. (a) Normalized average bond strength and (b) *in-situ* tensile strength of PE fiber in plain matrix M1 and in SHCC M1-PE including the exponential trendlines with the corresponding snubbing and strength reduction functions, respectively.
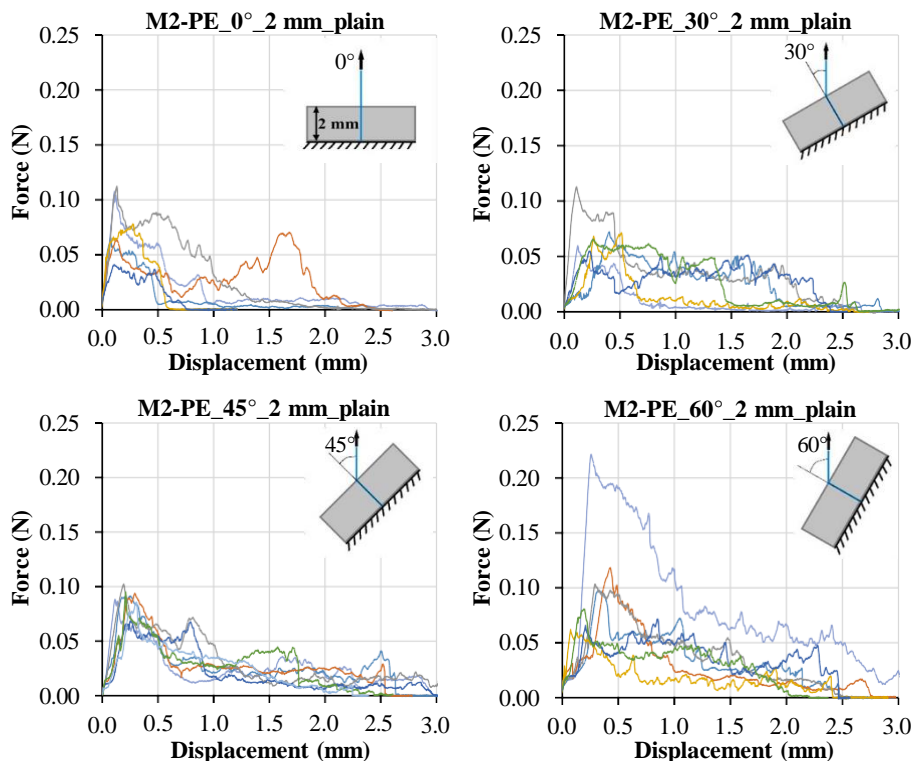

Fig. 12. Pullout curves of single PE fibers at different inclination angles in plain matrix M2. Embedded length is 2 mm.
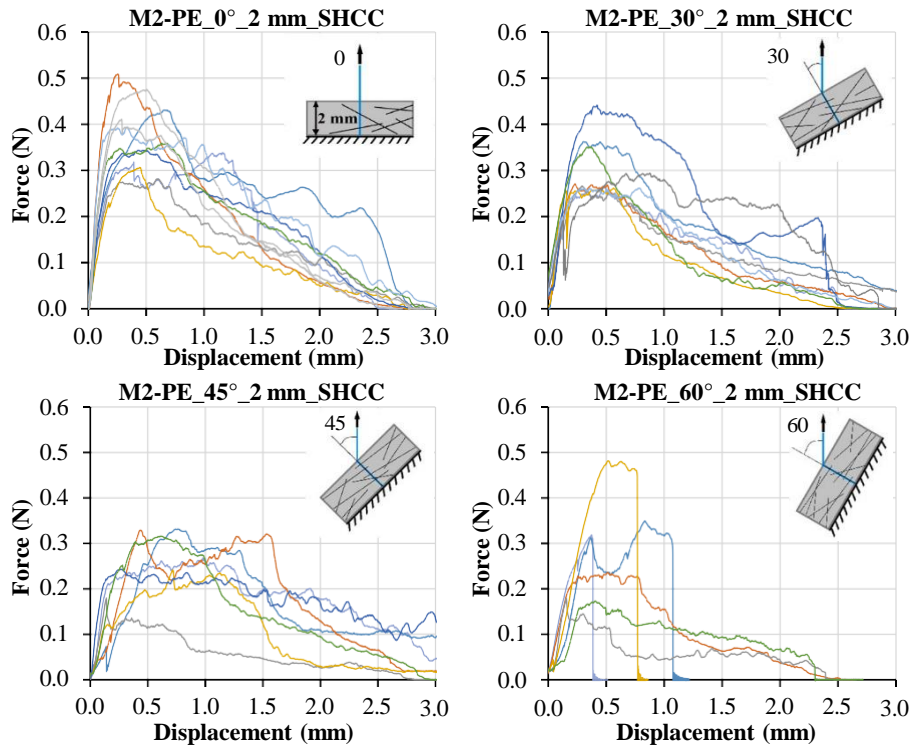
10

Fig. 13. Pullout curves of single PE fibers at different inclination angles in SHCC M2-PE with 1% fiber volume fraction. Embedded length is 2 mm.

Table 5

Frictional bond strength and *in-situ* tensile strength of PE fibers as a function of fiber inclination angle derived by means of single-fiber pullout experiments in plain matrix M2 and in SHCC M2-PE. Average values are given with standard deviations parentheses.

Parameter/fiber angle	0°	30°	45°	60°
τ_2 mm_plain in MPa	0 70 (0 24)	0 64 (0 18)	0 79 (0 09)	0 96 (0 48)
τ_2 mm_SHCC in MPa	3 41 (0 64)	2 68 (0 58)	2 41 (0 50)	2 56 (1 05)
τ_6 mm_plain in MPa	0 97 (0 40)	1 22 (0 36)[a]	1 26 (0 32)[a]	1 31 (0 34)[a]
σ_f_6 mm_plain in MPa	2274/–	1894 (345)	1889 (422)	1917 (317)
σ_f_6 mm_SHCC in MPa	2614 (510)	2422 (329)	2006 (440)	2109 (365)

[a] Also derived based on the fiber failure loads.

5.2. Fiber orientation in the miniature SHCC specimens

Fig. 15 presents 2D slices from reconstructed 3D volumes of the µCT scans together with segmented fibers from two representative M1-PVA specimens with $0°$ and 60° fiber inclination, respectively. Although the fibers clearly indicate preferential orientations, the alignment is not perfectly uniaxial, this being valid for all SHCC specimens investigated.

Two specimens per parameter combination were scanned and segmented, and the fiber inclination angles were derived relative to the longitudinal axes of the specimens. The discrete frequency distributions of the inclination angles in representative specimens are presented in Figure SI5 in SI for different types of SHCC. The frequency distributions of the fiber orientation angles presented in Figure SI5 were averaged for three representative specimens of different SHCC compositions and are presented in Fig. 16.

The statistical distributions of the inclination angles in the single-crack analytical models were generated according to continuous log-logistic functions, which were fitted to the experimental distributions
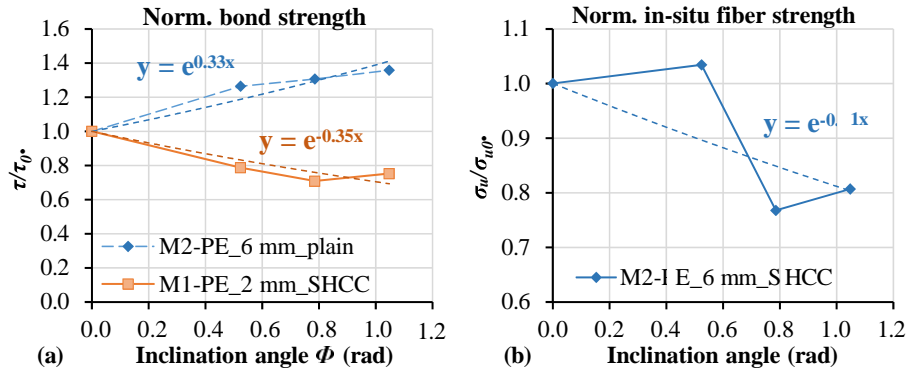

Fig. 14. (a) Normalized average bond strength and (b) *in-situ* tensile strength of PE fiber in plain matrix M2 and in SHCC M2-PE including the exponential trendlines with the resulting snubbing and strength reduction functions, respectively.
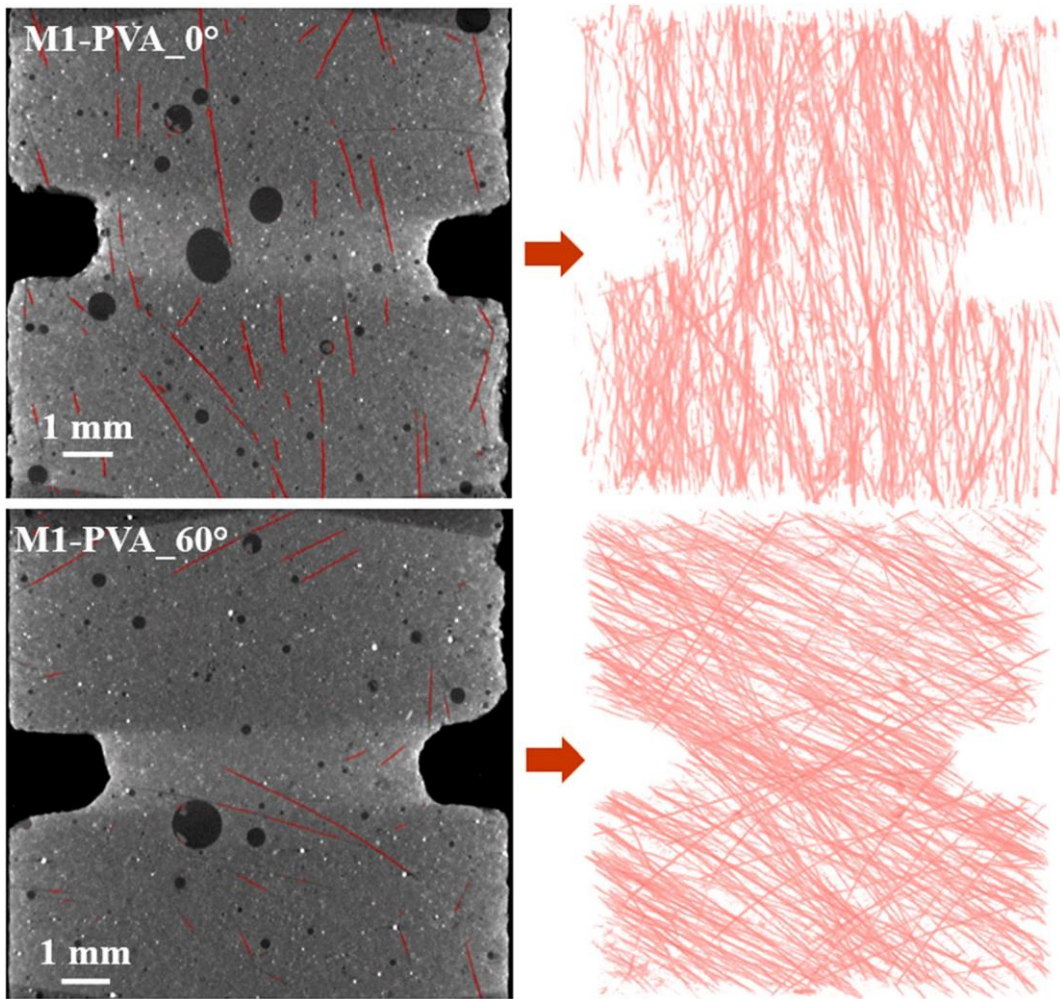
11

Fig. 15. Reconstructed 2D slices with segmented fibers (left) and 3D representation of the segmented fibers (right) of representative M1-PVA specimens with 0° and 60° fiber inclination.
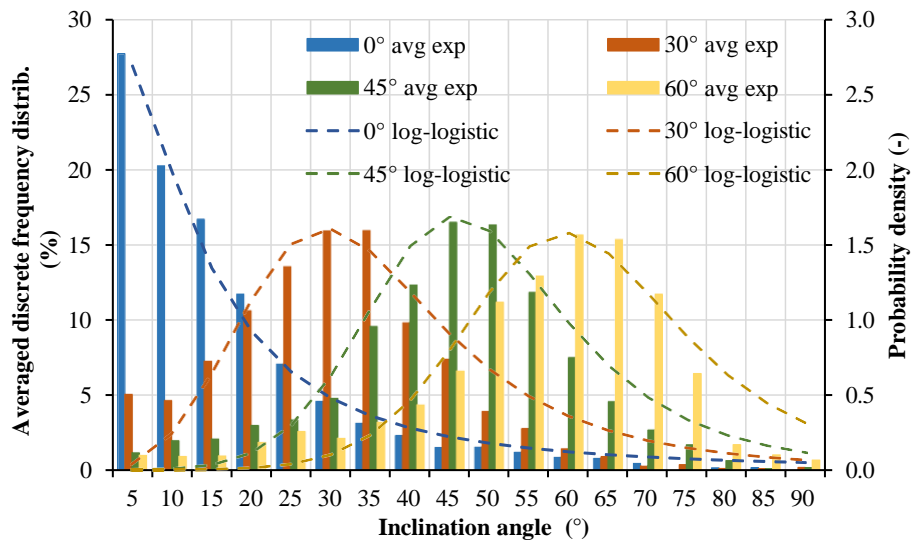

Fig. 16. Discrete frequency distributions of fiber inclination angles averaged for three SHCC specimens of different fiber-matrix combinations and equal target fiber orientations. The dashed curves indicate the fitting log-logistic probability density functions used in the analytical crack-bridging model.

and the values limited between 0° and 90°. The probability density function of the log-logistic distribution is given in Eq. (8):

$$F(x, \alpha, \beta) = \frac{(\beta/\alpha)(x/\alpha)^{\beta-1}}{(1 + (x/\alpha)^{\beta})_2} \quad (8)$$

where $\alpha > 0$ is the scale parameter and $\beta > 0$ is the shape parameter. These values are given in Section 6 for different specified fiber orientations.

The effective volume fraction of fiber was assessed in the vicinity of the notches, and the values demonstrate considerable scattering, ranging from 0.7% to 1.8%. However, with a voxel size of $(4.3^3\ \mu m^3)$, the cross-sectional shapes of the fibers could be only roughly recon- structed, and the derived fiber volume fraction could include a signifi- cant error. The same applies to the effective number of fibers in the middle cross-section. The microscopic analysis of the fracture surfaces did not enable the elucidation of this issue due to the transparent nature of the fibers, while ESEM would involve an exaggerated effort to count the fibers in the context of this work. For this reason the fiber volume fraction in the idealized analytical model was adopted as 1%. As well, the orientation-dependent numbers of fibers crossing the middle sec- tions were adjusted according to the function $\cos(\Phi)$ and not according to the segmentation data.

5.3. Tensile behavior of the miniature SHCC specimens

The titles of the diagrams in Figs. 17, 18, and 19 indicate the types of SHCC and the target fiber orientations. Despite the relatively low fiber volume fraction, the SHCC samples with longitudinally aligned fibers yielded tensile strength values notably higher than those achieved on specimens of common dimensions with 2% fiber volume content and random fiber orientation [29,30,31]. In addition to the axial fiber alignment in the 0° specimens, the small dimensions of the samples and the notches facilitated uniform crack opening at failure localization, which can hardly be achieved in specimens with larger cross-sections

and without notches. Note that due to the imperfect notch geometry and the resulting biaxial state of stress in the matrix, first-crack stress was not derived from the tension curves. Only the crack-bridging strength of the fibers was analyzed.

The curves of M1-PVA in Fig. 17 show a pronounced reduction in crack-bridging strength with increasing fiber inclination. While the curves corresponding to 0° inclination indicate a failure mode domi- nated by fiber rupture at larger crack openings, the tension curves cor- responding to the specimens with inclined fibers provide no evidence on the influence of inclination on the failure mode since the average dis- placements at peak load are identical and the crack-bridging vanishes at similar displacements in all diagrams; see Fig. 17.

The ESEM images in Fig. 18 show that the fracture surfaces of M1-PVA leave only short, protruding fiber ends, indicative of complete fiber rupture, and pronounced surface damage. In the case of 60° inclination, the fibers exhibit pronounced abrasive damage on the side remote from the snubbing edge, while large matrix fragments are attached to the fibers on the snubbing side, indicating pronounced cohesive failure and micro-spalling in the matrix. Nevertheless, the PVA fibers show no obvious radial deformations, and their preferential orientation in the case of 60° indicates elastic recovery despite the strong bending and surface damage occurring during crack opening; see Fig. 18b.

Considerably shallower descending branches with dominating fiber pullout can be observed in the case of M1-PE; see Fig. 19. The average tensile strength of M1-PE is larger than that of M1-PVA, which is a result of a considerably smaller fiber diameter, to wit: higher collective embedment surface, and higher fiber tensile strength. As opposed to M1- PVA, M1-PE yielded multiple cracking but, at the same time, pro- nounced scattering of the curves, which can be traced back to the infe- rior fiber dispersion, this being observed also in a former study [30].

M2-PE yielded the highest crack-bridging strength, whereas the softening branches corresponding to 0° inclination in Fig. 20 indicate a higher degree of fiber rupture in comparison to M1-PE. Thus, as opposed to M1-PE, the tensile strength of the PE fibers is properly exploited in
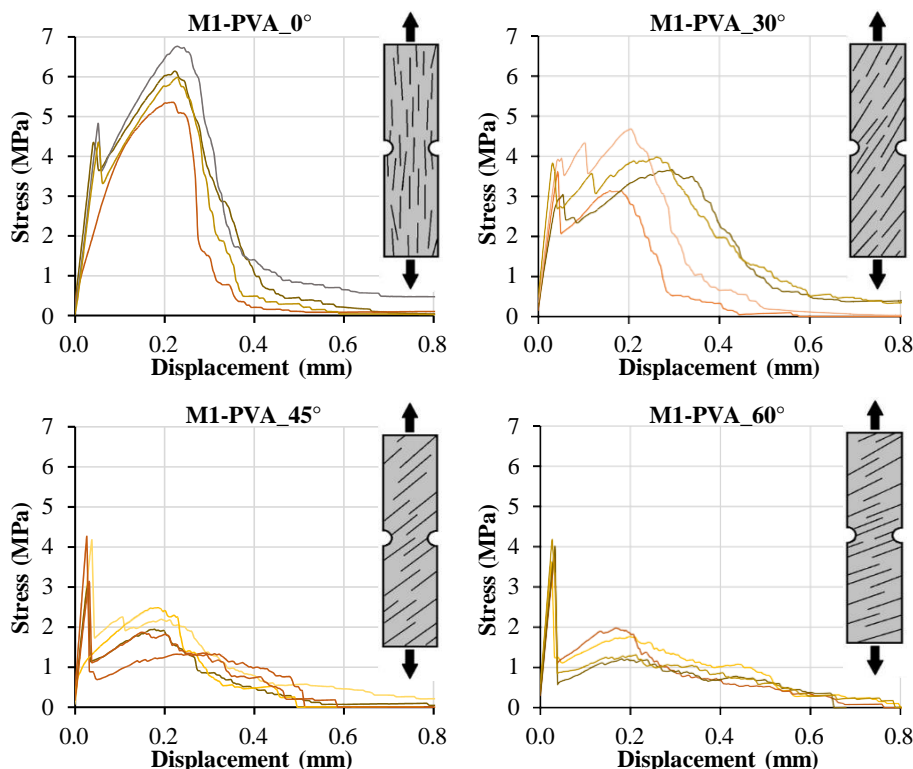

Fig. 17. Tensile stress-displacement curves of miniature M1-PVA specimens with different fiber orientations.
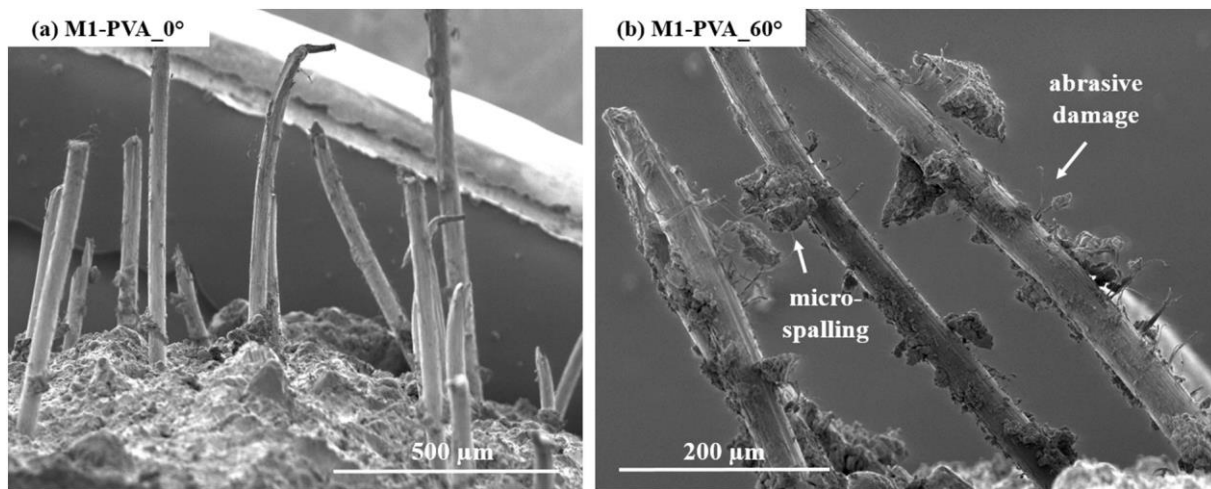
13

Fig. 18. ESEM images of the fracture surfaces of M1-PVA specimens with (a) 0° and (b) 60° fiber inclination. The crack-opening direction corresponds to the vertical axes of the ESEM images.
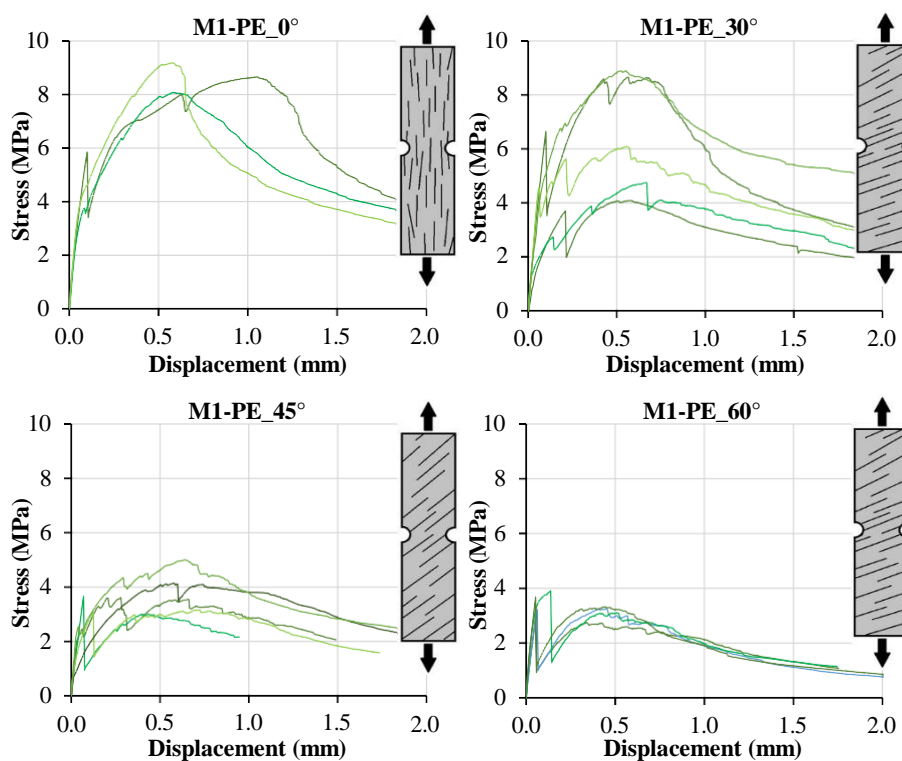

Fig. 19. Tensile stress-displacement curves of miniature M1-PE specimens with different fiber orientations.

M2. Both M1-PE and M2-PE yield a strong reduction in crack-bridging strength with increasing fiber inclination.

The ESEM images of the fracture surfaces of M1-PE and M2-PE at 0° demonstrate a high degree of fiber pullout in both cases with a limited degree of surface damage, not shown in this work. Interestingly, the PE fibers in M1 yielded more attached matrix fragments compared to those pulled out from M2, which can be attributed to the considerably lower strength and packing density of M1. These features can be observed in Fig. 21a, highlighting the large size of the fly ash particles compared to the diameter of the PE fibers and the relatively loose nature of the matrix surface, which also explains the cohesive bond failure in M1-PVA. As opposed to the PVA fibers, the inclined PE fibers in both M1-PE and M2-PE exhibit permanent flexural deformations and, at their exit points

from the matrix's buckled regions. Contrary to the 0° specimens, the M2-PE samples with 60° fiber orientation show severe fiber damage and more pronounced fiber rupture; see Fig. 21b.

As shown in Fig. 22, M1-PVA yielded more pronounced reductions in collective crack-bridging strength, while M1-PE and M2-PE showed a very similar trend with increasing fiber inclination. This could be traced back partly to the different failure modes depending on fiber type: fiber rupture for M1-PVA and mixed failure modes for M1-PE and M2-PE. Furthermore, the very similar trends of M1-PE and M2-PE agree with their similar snubbing and strength reduction coefficients, as derived in fiber reinforced specimens; see Figs. 11 and 14.

The snubbing coefficient and strength reduction coefficient derived in single-fiber pullout experiments exhibit a strong dependence on the
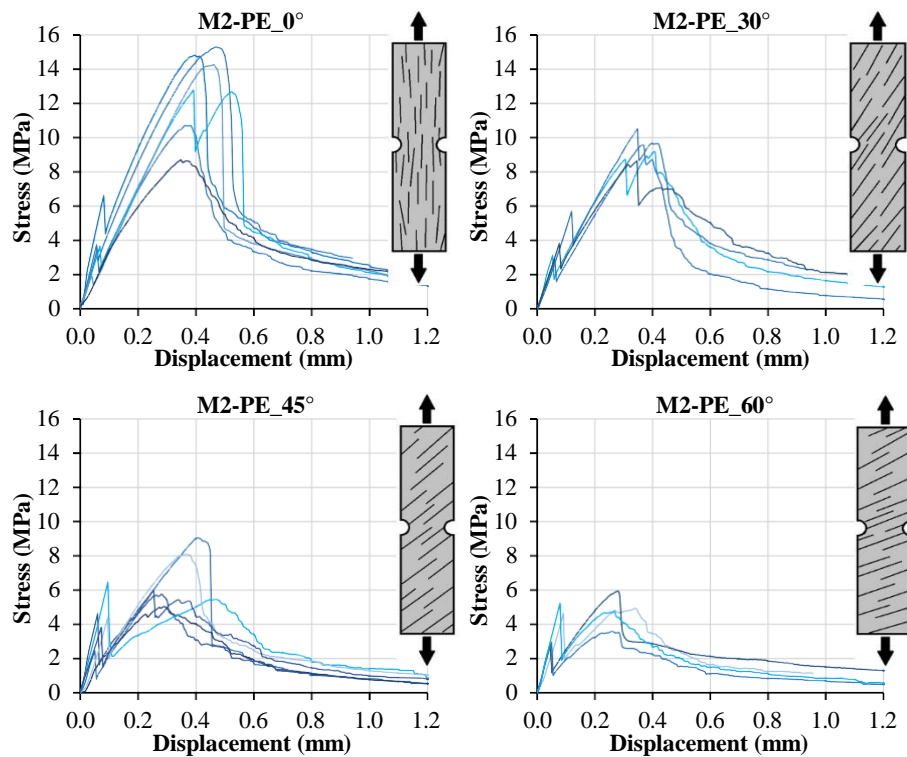
14

Fig. 20. Tensile stress-displacement curves of miniature M2-PE specimens with different fiber orientations.
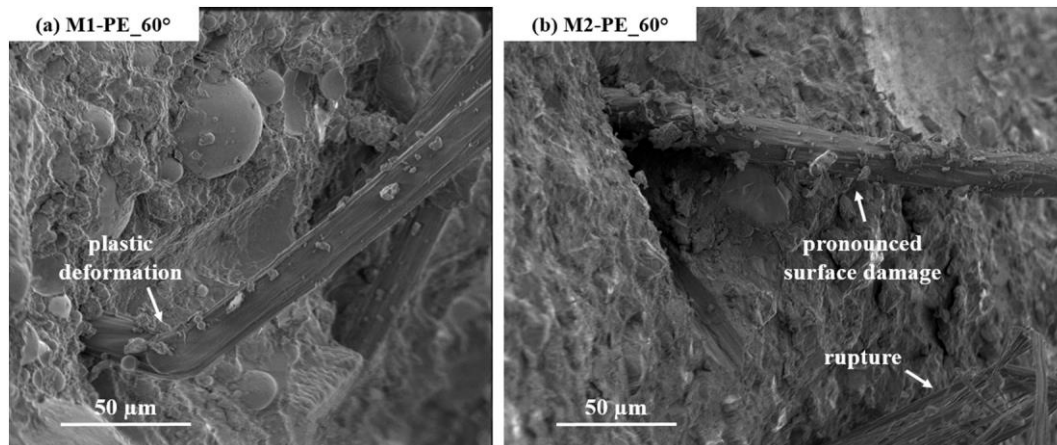

Fig. 21. ESEM images of the fracture surfaces of (a) M1-PE and (b) M2-PE specimens with 60° fiber inclination.

fiber-matrix combination, but also on the type of embedment material, *i. e.*, plain matrix or SHCC; see Section 5.1. As a result, these coefficients are not entirely consistent and, partially, even contradictory. Thus, their reliability in respect of upscaling accuracy can be only assessed by means of analytical modelling, as presented in Section 6, for which the normalized trends presented in Fig. 22b served as a reference experimental basis.

6. Analytical crack-bridging relationships

The input parameters of the analytical model are summarized in Table 6. The initial values for bond strength and fiber strength were adopted from micromechanical experiments on fiber reinforced pullout specimens as presented in Section 5.1. Due to the lack of statistical evidence, the fiber and bond strength were considered to be uniformly distributed between experimentally determined minimum and

maximum values. Such constant parameters as Young's modulus of the fiber E_f and Young's modulus E_m of the matrix were adopted from a previous study on identical materials [32]. Young's modulus of the fibers given in Table 6 is actually their secant stiffness up to peak load derived on fibers with 5 mm free length and, for reasons explained in [19], is considerably lower than the tangent Young's modulus provided by the producers. The chemical bond strength G_d and the slip-hardening modulus β_{sh} were adjusted in simulations on single fibers for matching the experimental pullout curves. The number of fibers generated by the model corresponds to an average specimen cross-section of 3.2 mm $\times$ 5.4 mm, as presented in Section 5.3. With a volume fraction of 1%, the number of fibers crossing the middle cross-sections in the case of 0° fiber orientation is 152 for M1-PVA and 679 for both M1-PE and M2-PE.

Note that neither the single-fiber pullout experiments nor the tension tests on SHCC specimens provided a reliable quantitative basis for assessing the influence of fiber inclination on the crack opening
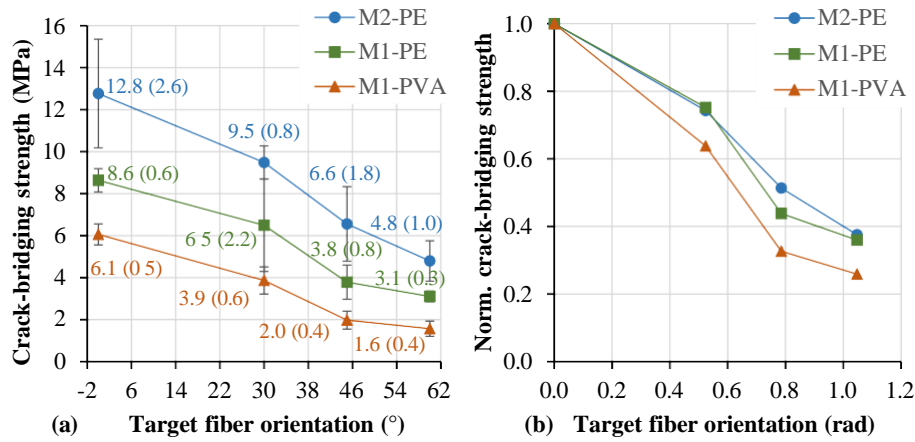
15

Fig. 22. Reduction of the collective crack-bridging strength of the SHCC under investigation as a function of fiber orientation (a) average values with standard deviations in parentheses and (b) normalized values.

Table 6
Input parameters in the analytical model, including their statistical distribution and ranges defined by the minimum and maximum values.

Parameter (unit)		Distribution	M1-PVA	M1-PE	M2-PE
In-situ σ_f (MPa)		Uniform	(451–743)	(1801–2922)	(2053–3211)
			800–1000*	1800–2520*	1800–2520*
E_f (GPa)		–	16	50	50
d_f (µm)		–	38	18	18
L_e (mm)		Uniform	0 1–6 0		
G_d (J/m²)		–	0 3–0 5	0 0	0 0
τ (MPa)		Uniform	(0 75–2 43)	(1 07–2 34)	2 71–4 50
			1 75–2 75*	0 8–1 4*	
β_{sh}		–	4 0	0 01	0 01
Φ (rad)		Log-logistic	α/β		
0 0000			0.223/1.429		
0 5236			0.600/3.571		
0 7854			0.852/5.556		
1 0472			1.083/6.667		
f (–)	In SHCC	–	0 27	−0.34	−0.35
	In plain matrix	–	−0.09	−0.73	0 33
f' (–)		–	0 00	0 18	0 21
E_m (GPa)		–	16 5	16 5	29 0

( ) from micromechanical experiments.
  * After adjustment for fitting the reference experimental curves.

displacement. Also, the model implies a simplified, linear representation of the fibers' stress-strain relationships whereas in reality they are non-linear. For this reason, the emphasis in this study is put on crack-bridging strength and not on crack-opening displacement (COD).

The assessment of the upscaling accuracy of the snubbing and strength reduction coefficients involved the consideration of the values
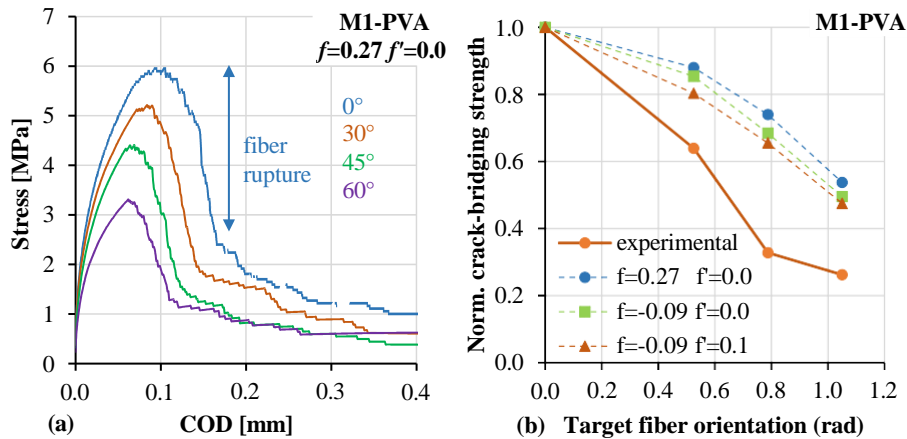

Fig. 23. (a) Representative crack-bridging curves of M1-PVA at different fiber orientations based on reference snubbing and strength reduction coefficients derived in SHCC embedment specimens. (b) Comparative assessment of the influence of snubbing and strength reduction coefficients to collective crack-bridging strength based on normalized trends.

16

are derived both in plain matrix and in SHCC; see Table 6. In this study, the snubbing coefficients derived in SHCC embedment specimens were adopted as reference and the analytical crack-bridging curves presented in Figs. 23a, 24a and 25a correspond to these coefficients. The influence of the snubbing coefficients derived based on plain matrix specimens are only presented comparatively in the normalized trend curves in Figs. 23b, 24b and 25b. The strength reduction coefficients were adopted based on the available data regardless of the embedment material.

The analytical simulations have a statistical character, and the crack-bridging laws generated yielded a certain scatter as determined by the distributions of the input parameters. For the sake of clarity, Figs. 23a, 24a and 25a show only representative curves of the simulations performed.

With the experimentally derived frictional bond strength and *in-situ* tensile strength of the PVA fibers in M1-PVA, the model predicted a collective crack-bridging strength of approximately 4 MPa in the case of longitudinal fiber orientation, not shown in this work. To achieve a better approximation of the experimental single-crack opening curves, the ranges of σ_f and τ were increased to 800 MPa–1000 MPa and 1.75 MPa–2.75 MPa, respectively. The initial input values are indicated in parentheses in Table 6 and the calibrated values are marked with *.

As opposed to M1-PVA, the strength of the PE fibers in M1-PE had to be reduced in the analytical model in order to approximate the experimental crack-bridging strength. In the case of M2-PE, the reduction of the *in-situ* fiber strength was not sufficiently high to match the experimental crack-bridging strength, but further reduction was avoided so as to maintain a certain quantitative proportion to the experimentally derived, micromechanical parameters.

The crack-bridging curves of M1-PVA relative to the crack-opening displacements (COD) as a function of fiber orientation are presented in Fig. 23a. The crack-bridging curves demonstrated decreases in both crack-bridging strength and crack-bridging stiffness with increasing fiber inclination. The pronounced fiber rupture is indicated by the abrupt post-peak stress drops. Given the relatively small number of crack-bridging fibers in the M1-PVA specimens, the individual rupture instances are evidenced by the small consecutive stress drops inthe post-peak phase.

Fig. 23b shows a pronounced discrepancy between the experimental and analytically derived reduction in crack-bridging strength with increasing fiber inclination. It also shows that the reduction strongly follows the theoretical decrease of the number of crack-bridging fibers according to cos(Φ). The adjustment of the snubbing coefficient according to the micromechanical results in plain matrix ($f = -0.09$ $f' = 0.0$) in Fig. 23b led to a minor increase in the reduction rate. However, this adjustment had a significant influence on the shape of the crack-

bridging curves and led to a strong increase in COD at peak stress compared to the curves in Fig. 23a and with increasing fiber inclination. The adjustment of the strength reduction coefficient to 0.1 led to a further increase of the strength reduction rate, but the influence is still minor with respect to the difference between the experimental and analytical trends. The presumable reason for such a discrepancy could be related to the difference between the actual decrease in the number of crack-bridging fibers and that defined by cos(Φ). Also, it might be assumed that the null strength reduction coefficients derived in the micromechanical experiments are not representative for the crack level in M1-PVA.

Fig. 24a shows that fiber rupture in the case of M1-PE is negligible and that the failure mode does not change with increasing fiber inclination. This is partly a result of the high margin between anchorage strength and fiber strength and of the negative snubbing coefficient as well. Also, as opposed to the analytical curves of M1-PVA, the strength reduction trend with increasing fiber orientation matches quite accurately the experimental trend; see Fig. 24b. The reduction of the snubbing coefficient to −0.73 according to the micromechanical results of plain matrix specimens resulted in a global reduction of the crack-bridging strength and in a larger deviation from the experimental trend up to 30° orientation but in a better approximation at larger fiber orientations. As this could be already observed in Figs. 8 and 11, the exponential snubbing and strength reduction coefficients do not enable the accurate matching of the experimental trends along the entire range of inclination angles, thereby preventing accurate assessment and exploitation of their accuracy.

Fig. 25a shows that M2-PE yields a considerable extent of fiber rupture, as can be judged by the abrupt post-peak stress drop. The larger snubbing coefficient when compared in absolute magnitude to the strength reduction coefficient leads to less pronounced fiber rupture with increasing fiber inclination. The adjustment of the snubbing coefficient from −0.35 as derived in SHCC to 0.33 as derived in plain matrix resulted in a strong reduction of crack-bridging strength with increasing fiber inclination, but in a lower rate of reduction; see Fig. 25b.

The analytical strength-reduction trend matches the experimental one less accurately than in the case of M1-PE; see Fig. 25b as compared to Fig. 24b. The difference in this case is that M1-PE exhibits considerably less fiber rupture, making the strength reduction coefficient of secondary importance. A further increase of the strength reduction coefficient to 0.50 compared to the reference case of M2-PE resulted in an accurate match with the experimental trend; see Fig. 25b. However, this adjustment also caused more pronounced fiber rupture and a reduction of the COD at peak stress with increasing inclination angles; *i.e.*, opposite the curves in Fig. 25a. It was observed in the case of M1-PVA and
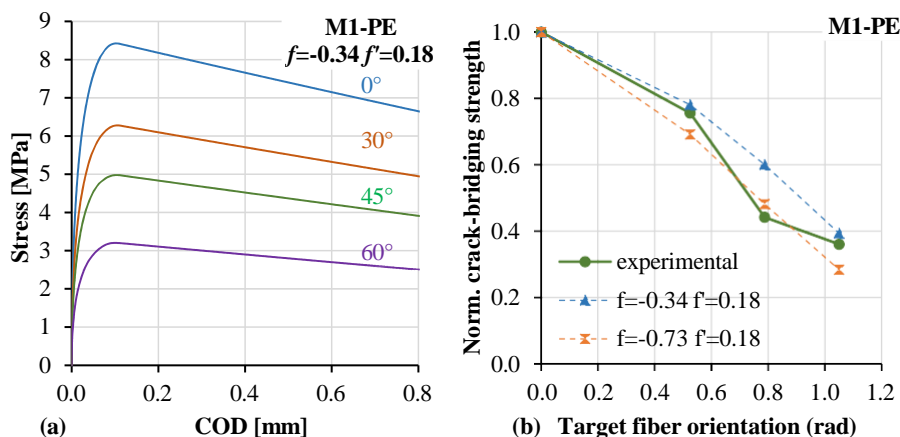

Fig. 24. (a) Representative crack-bridging curves of M1-PE at different fiber orientations based on reference snubbing and strength reduction coefficients derived in SHCC embedment specimens. (b) Comparative assessment of the influence of the snubbing and strength reduction coefficients on the collective crack-bridging strength based on normalized trends.

Fig. 25. (a) Representative crack-bridging curves of M2-PE at different fiber orientations based on reference snubbing and strength reduction coefficients derived in SHCC embedment specimens. (b) Comparative assessment of the influence of the snubbing and strength reduction coefficients on the collective crack-bridging strength based on normalized trends.
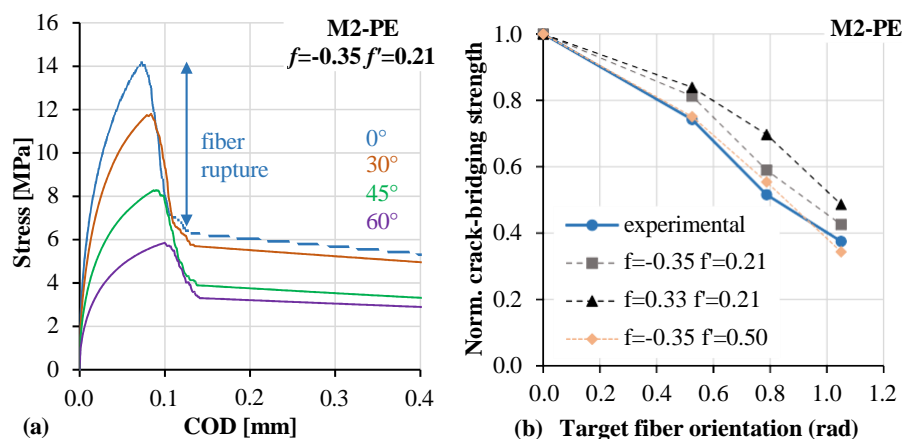
M2-PE that a positive snubbing coefficient results in a reduction of COD at peak stress with increasing fiber inclination, while a negative snubbing coefficient results in an opposite effect, given a constant strength reduction coefficient; see Figs. 23a and 25a. This can be traced back to the adjustment of the failure mode, in which a positive snubbing coefficient leads to more fiber rupture with increasing inclination angle. Thus, a dedicated experimental setup with an accurate monitoring of the CODs would facilitate a more accurate assessment of the snubbing coefficients by applying the analysis of the crack widths additionally into that of crack-bridging strength.

The scale-linking experiment-model comparison indicates that the influence of fiber orientation on the tensile properties of SHCC depends strongly on the material composition. The accuracy of the experimentally derived snubbing and strength reduction coefficients in predicting the collective crack-bridging relationships is limited by their high sensitivity against the testing conditions, embedded length and material. Also, the micromechanical experiments and analytical models do not reflect all the crack-bridging mechanisms typical for SHCC, such as matrix spalling, bending of the fibers, fiber rupture inside the embedment channel, which indicates further refinement potential for both the micromechanical testing configurations and the analytical models.

7. Conclusions and outlook

A scale-linking experimental study was carried out to investigate the influence of fiber orientation on the crack-opening relationships of three SHCC compositions, these being normal-strength and high-strength matrices as common combinations examined with PVA and PE fibers. Compared to the published studies on this matter, the single-fiber pullout experiments in this study suggested an improved testing configuration in terms of fiber inclination. The pullout tests were additionally performed with dispersed fibers in the embedment specimens in order to reproduce the embedment conditions of the fibers in SHCC. The inclination angles investigated in the pullout experiments at the single fiber level and at the composite scale, *i.e.*, in tension tests on SHCC, were 0°, 30°, 45° and 60°. Miniature SHCC specimens with tailored geometry and controlled fiber orientations were tested under uniaxial tension. The effective fiber orientation in the SHCC specimens was quantitatively evaluated by means of a deep-learning semantic fiber segmentation of reconstructed X-ray μCT scans. The experimentally derived micromechanical properties, together with the data on fiber orientation in the SHCC specimens, served as input into an analytical crack-bridging model whose output in terms of crack-bridging relationships was compared to the tensile curves of the notched SHCC specimens, in this way enabling a direct assessment of the accuracy of the

micromechanical parameters with emphasis on the snubbing and strength reduction coefficients.

The improved configuration of the single-fiber pullout specimens and experiments involving constant fiber embedment and specimen rotation in the machine instead of fiber rotation in the embedment piece facilitated an accurate assessment of the effect of inclination angle on the bond properties despite the pronounced scattering of the micromechanical results. The single-fiber pullout experiments on specimens with PE fibers clearly showed that the dispersed fibers in the embedment specimens have a strong effect on the fibers' bonding properties compared to those embedded in plain matrix. This effect was related to the increased specific surface of the system and limited micro-bleeding at the fiber surface. Due to their hydrophilic nature, the PVA fibers' anchoring strength did not show any difference between the plain matrix and the SHCC.

The occurrence of fiber rupture and matrix spalling with increasing inclination angle in the pullout experiments hindered the accurate derivation of the bond properties and of the snubbing and strength reduction coefficients along the entire range of the inclination angles investigated. Furthermore, these coefficients reveal themselves as highly sensitive to the type of embedment material, *i.e.*, plain or fiber reinforced matrix, hence resulting in inconsistent and partially contradictory results. For this reason, the data derived in fiber reinforced specimens were adopted as reference in the analytical model. It could be demonstrated that the effect of fiber orientation on pullout behavior depends strongly on the fiber-matrix combination. Contrary to the results reported so far, the PE fibers exhibited an obvious negative snubbing coefficient both in the normal-strength and high-strength matrices.

The μCT analysis accompanied by the deep learning segmentation of the fibers provided a detailed three-dimensional quantification of fiber distribution and orientation in the SHCC specimens. These data served as an important basis for a more accurate experiment-model comparison. Regarding the influence of fiber orientation, the analytical crack-bridging model yielded an accurate match to the experimental results of both PE-SHCC but did not accurately predict the reduction in crack-bridging strength in the case of normal-strength SHCC with PVA fibers. This indicates that the micromechanical experiments are not sufficient to mirror the effects of fiber orientation on the collective crack-bridging properties accurately and that there are additional mechanisms, such as matrix spalling, which should be considered as well. Also, additional to crack-bridging strength, the accurate monitoring of crack-opening displacements in the tension experiments on SHCC would facilitate a more detailed comparison of the experimental and analytical results.

CRediT authorship contribution statement

IC – conceptualization, methodology, supervision, data curation, investigation, formal analysis, validation, visualization, writing – original draft, writing – review & editing.

EM – methodology, data curation, writing – review & editing.

MI – methodology, data curation, formal analysis, visualization, writing – review & editing.

AHA – data curation, formal analysis, writing – review & editing.

ML – data curation, formal analysis, visualization, writing – review & editing.

VM – funding acquisition, project administration, resources, supervision, writing – review & editing.

Declaration of competing interest

I hereby confirm that this publication has been approved by all co-authors, as well as – tacitly or explicitly – by the responsible author- ities at the institution where the work was carried out. The corre- sponding author signs for and accepts responsibility for releasing this material on behalf of any and all co-authors. All financial sources and grants have been disclosed.

Acknowledgments

Appendix A. Supplementary data

Supplementary data to this article can be found online at https://doi.org/10.1016/j.cemconres.2021.106650.

References

[1] V C Li, On engineered cementitious composites (ECC): a review of the material and its applications, J Adv Concr Technol 1 (3) (2003) 215–230

[2] V C Li, From micromechanics to structural engineering – the design of cementitious composites for civil engineering applications, J Struct Mech Earthq Eng 10 (1993) 37–48

[3] C V Li, D Mishra, A Naaman, J Wight, J M LaFave, H C Wu, Y Inada, On the shear behavior of engineered cementitious composites, Adv Cem Based Mater (1994) 142–149

[4] C Ding, L Guo, B Chen, Orientation distribution of polyvinyl alcohol fibers and its influence on bridging capacity and mechanical performances for high ductility cementitious composites, Constr Build Mater 247 (2020), 118491

[5] T Kanakubo, M Miyaguchi, K Asano, Influence of fiber orientation on bridging performance of polyvinyl alcohol fiber-reinforced cementitious composite, ACI Mater J 113 (2) (2016) 131–141

[6] H Ogura, V N Nerella, V Mechtcherine, Developing and testing of strain-hardening cement-based composites (SHCC) in the context of 3D-printing, Materials 11 (8) (2018) 1375

[7] V C Li, F P Bos, K Yu, W McGee, T Y Ng, S C Figueiredo, K Nefs, V N Mechtcherine, J Pan, P A G van Zijl, P J Kruger, On the emergence of 3D printable engineered, strain hardening cementitious composites (ECC/SHCC), Cem Concr Res 132 (2020), 106038

[8] H Zhu, K Yu, V C Li, Sprayable engineered cementitious composites (ECC) using calcined clay limestone cement (LC3) and PP fiber, Cem Concr Compos 115 (2021), 103868

[9] V C Li, Y Wang, S Backer, Effect of inclining angle, bundling, and surface treatment on synthetic fibre pull-out from a cement matrix, Composites 21 (2) (1990) 132–140

[10] C K Y Leung, V C Li, Effect of fiber inclination on crack bridging stress in brittle fiber reinforced brittle matrix composites, J Mech Phys Solids 40 (6) (1992) 1333–1362

[11] C K Y Leung, N Ybanez, Pullout of inclined flexible fiber in cementitious composite 123 (3) (1997) 239–246

[12] T Kanda, V C Li, Interface property and apparent strength of a high strength hydrophilic fiber in cement matrix 10 (1) (1998) 5–13

[13] C Wu, Micromechanical Tailoring of PVA-ECC for Structural Application, PhD Thesis, University of Michigan, 2001

[14] Y Ozu, H Yamada, A Yasojima, T Kanakubo, Evaluation of shear and tensile bridging characteristics of PVA fibers based on bridging law, in: V Mechtcherine (Ed), Proceedings of the IVth International Conference on Strain-hardening Cement-based Composites (SHCC4), 18-20 September 2017, Dresden, Germany, Springer, Netherlands, 2017, pp 89–96, 978-94-024-1194-2

[15] R Ranade, V C Li, W F Heard, Tensile rate effects in high strength-high ductility concrete, Cem Concr Res 68 (2015) 94–104

[16] D Y Lei, L P Guo, J P Li, B Chen, D X Li, S C Li, V Mechtcherine, Micro-mechanical model for ultra-high strength and ultra-high ductility cementitious composites (UHS-UHDCC), Constr Build Mater 267 (2021), 120668

[17] Effects of embedment length and angle of PVA-fibers on tensile performance of FRC, in: V Mechtcherine (Ed), Proceedings of the IVth International Conference on Strain-hardening Cement-based Composites (SHCC4), 18-20 September 2017, Dresden, Germany, Springer, Netherlands, 2017, pp 79–87, 978-94-024-1194-2

[18] I Curosu, M Liebscher, V Mechtcherine, C Bellmann, S Michel, Tensile behavior of high-strength strain-hardening cement-based composites (HS-SHCC) made with high-performance polyethylene, aramid and PBO fibers, Cem Concr Res 98 (2017) 71–81

[19] I Curosu, M Liebscher, G Alsous, E Muja, H Li, V Mechtcherine, A Drechsler, R Frenzel, A Synytska, Tailoring the crack bridging behavior of strain-hardening cement-based composites (SHCC) by chemical surface modification of poly(vinyl alcohol) (PVA) fibers, Cem Concr Compos 114 (2020), 103722

[20] J Zhang, V C Li, Effect of inclination angle on fiber rupture load in fiber reinforced cementitious composites, Compos Sci Technol 62 (2002) 775–781

[21] C Lu, C K Y Leung, Theoretical evaluation of fiber orientation and its effects on mechanical properties in engineered cementitious composites (ECC) with various thicknesses, Cem Concr Res 95 (2017) 240–246

[22] C Wu, C K Y Leung, V C Li, Derivation of crack bridging stresses in engineered cementitious composites under combined opening and shear displacement, Cem Concr Res 107 (2018) 253–263

[23] J Yao, C K Y Leung, A new physical model for empirical fiber snubbing effect in cementitious composites based on large deflection beam theory, Cem Concr Compos 96 (2019) 238–251

[24] R Lorenzoni, I Curosu, F Leonard, S Paciornik, V Mechtcherine, F A Silva, G Bruno, Combined mechanical and 3D-microstructural analysis of strain-hardening cement-based composites (SHCC) by in-situ X-ray microtomography, Cem Concr Res 136 (2020), 106139

[25] R Lorenzoni, I Curosu, S Paciornik, V Mechtcherine, M Oppermann, F A Silva, Semantic segmentation of the micro-structure of strain-hardening cement-based composites (SHCC) by applying deep learning on micro-computed tomography scans, Cem Concr Compos 108 (2020), 103551

[26] Kuraray Co Ltd , Kuralon K II high tenacity type fibers http://www kuraray co jp/kii/english/, 2018 (accessed April, 2021)

[27] Fact Sheet, Ultra High Molecular Weight Polyethylene Fiber From DSM Dyneema, Eurofibers, 2010 (accessed April, 2021), https://issuu com/eurofibers/docs /name8f0d44

[28] M Ranjbarian, V Mechtcherine, Z Zhang, I Curosu, J Storm, M Kaliske, Locking front model for pull-out behavior of PVA microfibre embedded in cementitious matrix, Cem Concr Compos 103 (2019) 318–330

[29] I Curosu, S Pirskawetz, V Mechtcherine, Characterizing the crack development in strain-hardening cement-based composites (SHCC) by means of acoustic emission, in: V Saouma (Ed), 9th International Conference on Fracture Mechanics of Concrete and Concrete Structures FraMCoS-9, Berkeley, California, USA, 2015, https://doi org/10 21012/FC9 207

[30] I Curosu, V Mechtcherine, O Millon, Effect of fiber properties and matrix composition on the tensile behavior of strain-hardening cement-based composites (SHCCs) subject to impact loading, Cem Concr Res 82 (2016) 23–35

[31] I Curosu, V Mechtcherine, D Forni, E Cadoni, Performance of various strain-hardening cement-based composites (SHCC) subject to uniaxial impact tensile loading, Cem Concr Res 102 (2017) 16–28

[32] I Curosu, Influence of Fiber Type and Matrix Composition on the Tensile Behavior of Strain-hardening Cement-based Composites (SHCC) Under Impact Loading, Doctoral Thesis, Schriftenreihe des Instituts für Baustoffe Heft 2018/1, V Mechtcherine (Hrsg), TU Dresden, 2018 ISBN 978-3-86780-555-1

[33] A Drechsler, R Frenzel, A Caspari, S Michel, M Holzschuh, A Synytska, I Curosu, M Liebscher, V Mechtcherine, Surface modification of poly(vinyl alcohol) fibers to control the fiber-matrix interaction in composites, Colloid Polym Sci 297 (7) (2019) 1079–1093

[34] E -H Yang, S Wang, Y Yang, V C Li, Fiber-bridging constitutive law of engineered cementitious composites, J Adv Concr Technol 6 (1) (2008) 181–193

[35] W P Boshoff, V Mechtcherine, G P A G Van Zijl, Characterising the time-dependant behaviour on the single fibre level of SHCC: part 2: the rate effects on the fibre pull-out tests, Cem Concr Res 39 (2009) 787–797

[36] A Shehni, U Ha¨ußler-Combe, I Curosu, T Gong, V Mechtcherine, Numerical simulation of HS-SHCC under quasi-static tensile loading, in: G Pijaudier-Cabot, et al (Eds), 10th International Conference on Fracture Mechanics of Concrete and Concrete Structures FraMCoS-X,Bayonne, France, 2019, https://doi org/ 10 21012/FC10 233164

[37] V C Li, C K Y Leung, Steady-state and multiple cracking of short random fiber composites, J Eng Mech 118 (11) (1992) 2246–2264

[38] E -H Yang, V C Li, Strain-hardening cement optimization and component tailoring by means of micromechanical model, Constr Build Mater 24 (2010) 130–139

[39] M Maalej, V C Li, T Hashida, Effect of fiber rupture on tensile properties of short fiber composites, J Eng Mech 121 (8) (1995) 903–913

[40] P Jun, V Mechtcherine, Behaviour of strain-hardening cement-based composites (SHCC) under monotonic and cyclic tensile loading, part 2 – modelling, Cem Concr Compos 32 (2010) 801–809

[41] V C Li, Y Wang, S Backer, A micromechanical model of tension-softening and bridging toughening of short random reinforced brittle matrix composites 39 (5) (1991) 607–625

[42] Z Lin, V C Li, Crack bridging in fiber reinforced cementitious composites with slip-hardening interfaces 45 (5) (1997) 763–787

[43] Z Lin, T Kanda, V C Li, On interface property characterization and performance of fiber-reinforced cementitious composites, Concr Sci Eng 1 (1999) 173–184

[44] S Zhandarov, E Pisanova, B Lauke, Is there any contradiction between the stress and energy failure criteria in micromechanical tests? Part I Crack initiation: stress-controlled or energy controlled? 5 (5) (1997) 387–404